

#3

## End-of-the Fiscal-Year Summary Report for 1994

### Contract Information

R&T Number: 4322480  
Contract/Grant Title: N00014-89-J-1361/Basic studies in turbulent shear flows  
Scientific officer: Dr. L. P. Purtell  
Principal investigator: Fazle Hussain  
Mailing address: University of Houston Mechanical Engineering Dept. 77204-4792  
Phone number: (713) 743-4545  
Fax number: (713) 743-4544  
E-Mail address: mecelw@jetson.uh.edu

### A. Description of the Scientific Research Goals

The goal of this research is to understand the underlying physics of turbulence phenomena through coherent structures (CS). The aim is not only to understand the flow physics but also to devise methods for turbulence prediction and control. Our approach utilizes experiment, numerics and theory to understand both CS dynamics and structure. CS are studied in two ways: (i) long-time, global dynamics using experimental data and dynamical systems theory and (ii) crucial, localized CS interactions understood via vorticity dynamics. Below, we have summarized results in several key areas: (i) global dynamics in a forced plane mixing layer (ii) ODE models for spatially developing free shear flows, (iii) core dynamics and transition in a plane mixing layer, (iv) vorticity and helicity statistics in a circular jet, (v) new approaches to identifying sources of jet noise, and (vi) the kinematic separation of homogeneous mixtures.



This document has been approved  
for public release and sale; its  
distribution is unlimited.

Accession For	
NTIS CRA&I	<input checked="" type="checkbox"/>
DTIC TAB	<input type="checkbox"/>
Unannounced	<input type="checkbox"/>
Justification	
By <b>A247420</b>	
Distribution /	
Availability Codes	
DA	Avail and/or Special
<b>A-1</b>	

19941227 003

## B. Significant Results in the Past Year

### 1. Global dynamics in a forced plane mixing layer

A temporal dynamical systems description to identify low-dimensional temporal dynamics in closed/open flows is inappropriate (perhaps useless) unless existence of *global* modes is established. This problem is particularly relevant to *open* flows (such as jets, mixing layers and boundary layers) which are technologically relevant and whose locally convectively unstable nature makes them sensitive to external noise. The objective of this study was to provide an approach ca-

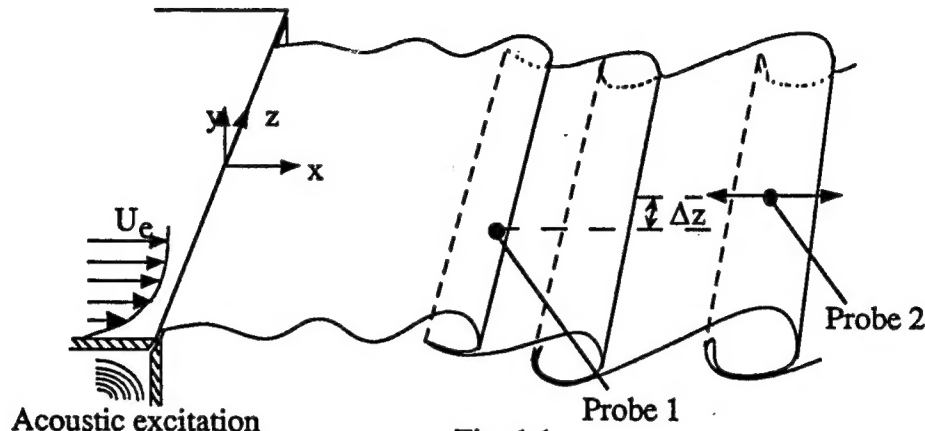


Fig. 1.1

pable of detecting global dynamics in an open flow and of determining its spatial extent. The experiments were performed in a newly built, carefully documented, quiet (free-stream turbulence intensity  $u'/U_e \leq 0.1\%$ ), laminar, plane ML facility (see figure 1.1) in our anechoic chamber; single-frequency forcing was provided at the lip (Narayanan 1994). The temporal attractors were briefly analyzed earlier, and the following results and discussions focus more on the studies of their spatial extents.

**Temporal dynamics** The low-dimensional dynamical states in the control parameter space are depicted in a phase diagram (see figure 1.2). The evolution and interactions of rolled-up and paired vortices together with feedback from these vortices to the origin constitute the mixing layer *global* dynamics; velocity signals were recorded for  $0.008\% \leq a_f \leq 1\%$  and  $0.006 \leq St_{\theta e} \leq 0.02$ . The control parameters used were:  $St_{\theta e} (\equiv f_{ex} \theta_e / U_e, U_e = \text{exit velocity and } f_{ex} = \text{excitation frequency})$  and  $a_f (\equiv u'_f / U_e, \text{the peak rms-velocity fluctuation at } f_{ex} \text{ recorded at the lip})$ . A periodic attractor, stable double pairing (SDP), is found at *all*  $St_{\theta e}$  and sufficiently high  $a_f$ . The period-2 limit cycle (see figure 1.2b) has a dimension  $\nu \approx 1.18$  (for an embedding dimension  $m = 3$ ) and  $\lambda \approx 0$  bpo. For lower  $a_f$ , the stable pairing (SP) attractor is found which has a periodic appearance (*i.e.*,  $\nu \approx 1.3$ ) at large phase-space scales and chaotic behavior (*i.e.*,  $\nu \approx 2$  and  $\lambda > 0$ ) at small phase-space scales; its identity therefore remains unresolved. For even lower  $a_f$ , two chaotic states, the quarterharmonic chaotic attractor (QCA, for  $St_{\theta e} \geq 0.0115$ ) and the subharmonic chaotic attractor (SCA, for  $St_{\theta e} < 0.0115$ ), were found for two different ranges of  $St_{\theta e}$  which appear via an apparent *intermittency* transition (denoted as INT in figure 1.2a). QCA is characterized by periodic vortex roll-up followed by a nearly periodically modulated first pairing

and a chaotic second pairing. Its phase portrait (see figure 1.2c) and the absence of tight and well-separated clusters in its Poincaré section are expected for a chaotic attractor for which we find  $\nu \approx 2.43$  ( $m = 4$ ) and  $\lambda \approx 0.32$  bpo. SCA involves periodic roll-up followed by aperiodic modulations of the first pairing; we find  $\nu \approx 2.2$  and  $\lambda \approx 0.09$  bpo, indicating chaotic behavior.

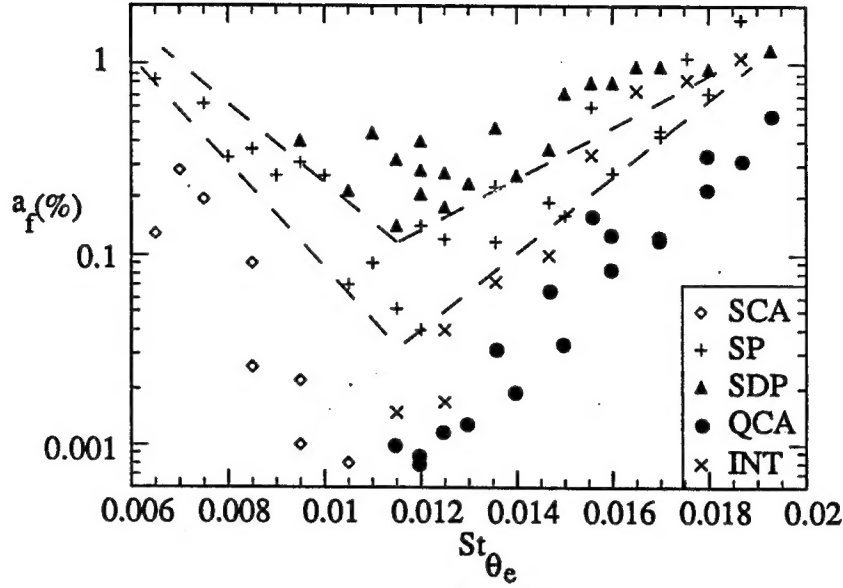


Fig. 1.2a

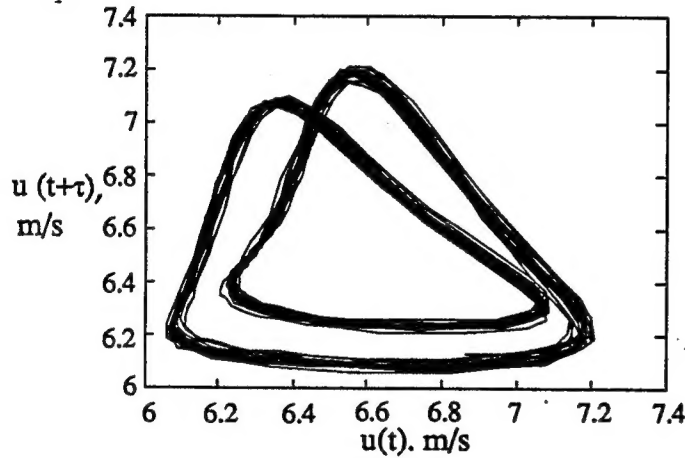


Fig. 1.2b

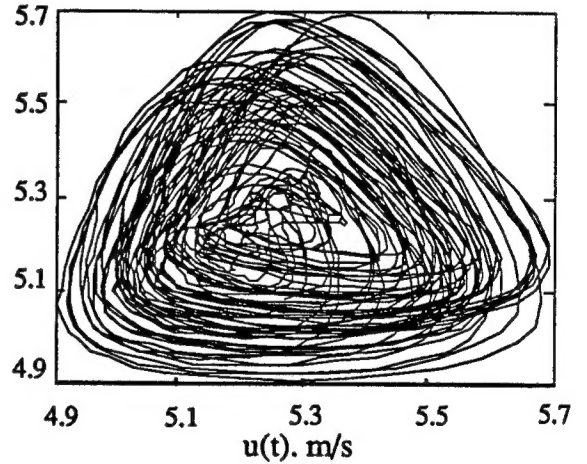


Fig. 1.2c

Interestingly, at  $St_{\theta e} \approx 0.0115$ , the  $a_f$  required to achieve SP and SDP (indicated roughly by dashed lines in figure 1.2a) has a minimum; we believe this to be supportive evidence of feedback in the mixing layer. For very low  $a_f$ , some aperiodically modulated states are found for which dimension calculation results are inconclusive. Further details of these states and their transitions can be found in Narayanan (1994).

**Spatial characteristics** We used spatial measurements to determine the presence/absence of global dynamics and discuss them in the following. When global dynamics is present, spatially separated points in a flow domain are *coupled*; i.e., dynamics at different locations depend on each

other. When global dynamics is disrupted (*i.e.*, it is weak or absent), different points lose spatial coupling, and the resulting dynamics is called *spatiotemporal*. This "loss of spatial coupling" can come from temporal chaos due to extreme sensitivity to initial conditions; *i.e.* points very close in phase-space diverge exponentially from each other, and will also result in *spatial* disorder. Since small differences in the initial conditions are amplified resulting in spatially uncoupled dynamics, this behavior could be termed *spatiotemporal chaos*. We have determined coherence and cross-bicoherence to be appropriate spatial measures (Narayanan 1994), as opposed to conventionally used (in homogeneous flows) cross-correlation. This is because spatially developing flows are inhomogeneous (*i.e.*, their local dynamics vary in space), causing correlation to decay *rapidly* while the dynamics at different locations may yet be spatially coupled.

The evolution of peak coherence, cross-bicoherence and relative phase at dynamically significant frequencies resulting from forced roll-up and periodic/modulated first and second pairings was examined for SDP and QCA, up to locations beyond that of the second pairing.

For SDP, coherences at the fundamental, the subharmonic and the quarterharmonic remain high ( $\geq 0.9$ ) for  $x/\theta_e \leq 300$ , and are accompanied by linear variations of the averaged relative subharmonic phase indicating phase coherent signals. Cross-bicoherences for the fundamental-subharmonic (f-s) interaction were high, indicating strong resonance, as expected for a stable first pairing, and the cross-bicoherence levels for the subharmonic-quarterharmonic (s-q) interaction were also high ( $\geq 0.9$ ) beyond the first pairing location ( $x/\theta_e \approx 110$ ) where the second pairing is initiated due to the second resonance. Thus, *spatially coherent motion* extending beyond the second pairing location is found, and even though the flow is *physically open*, dynamics of spatially separated points are strongly coupled over a few instability wavelengths ( $x/\lambda_f \geq 7$ ); the latter feature indicates a global mode.

For QCA, coherences at the fundamental  $f$ , the lower sideband  $f_l$ , the higher sideband  $f_h$  and the quarterharmonic remain high ( $\geq 0.7$ ) up to  $x/\theta_e \approx 180$ , where chaotic second pairing occurs. High levels of cross-bicoherence ( $\geq 0.8$ ) for the  $f$ - $f_l$  and  $f$ - $f_h$  interactions is observed for  $80 \leq x/\theta_e \leq 180$  indicating spatial coupling up to the completion of the first pairing, but it decays rapidly thereafter. Beyond  $x/\theta_e \approx 180$ , coherences at all significant frequencies and cross-bicoherences for any triad of frequencies decay rapidly; this indicates progressive loss of spatial coupling between the origin and the downstream locations, implying the onset of spatiotemporal dynamics. Thus, before the second pairing ( $x/\lambda_f \approx 6$ ,  $x/\theta_e \approx 180$ -230) strong spatial coupling is evidenced. The relative phases at individual frequencies show nearly linear variation of phase with  $x$  supporting the claim of phase coherence at the sidebands up to  $x/\theta_e \approx 160$ , but nonlinear variations (with  $x$ ) in the quarterharmonic phase due to its chaotic dynamics. Highly coherent behavior in the first pairing region indicates that although the instantaneous subharmonic phase at a fixed location varies, due to shifting of the downstream pairing location, its phase is well coupled to that at the origin. The chaotic second pairing also provides feedback at aperiodic intervals causing the quarterharmonic phase at the origin ( $\phi_q$ ) to vary. But, in contrast to the first pairing, decaying coherence & cross-bicoherence during second pairing reflects a quarterharmonic phase that is poorly matched with  $\phi_q$ ; we term this *phase incoherence*.

Coherences at the fundamental (a broadband around  $St_{\theta_e} \approx 0.01$ ) and the subharmonic (a broadband around  $St_{\theta_e} \approx 0.0055$ ) were recorded for the unforced ML and remain above 0.9 up to  $x/\theta_e \approx 120$ , *i.e.* after completion of roll-up, but decays thereafter. It is surprising that the coherence at the aperiodic subharmonic remains at  $\gamma^2(f/2) \geq 0.7$  for  $150 \leq x/\theta_e \leq 220$  (indicating *some* spatial coupling), where an aperiodic first pairing occurs. Since coupling reflects presence of a global mode, the *limited* spatial coupling shown by moderate subharmonic coherence during pairing suggests that the unforced ML has a *weak* global mode, *i.e.*, finite amplitude disturbances can trigger a global instability. Therefore, we expect that with external forcing, global modes will be established, and this is consistent with our experiments where finite  $a_f$  triggers periodic pairing. **Spatial evolution of temporal attractors** To study the spatial development of the temporal attractors, correlation dimension ( $v$ ), and largest Lyapunov exponent ( $\lambda$ ) were computed from SDP and QCA signals sampled at different streamwise locations from upstream of roll-up to downstream of the second pairing. In SDP, for most of the streamwise extent  $v \approx 1.1-1.2$  ( $m = 3$ ) with  $\lambda \approx 0$  bpo, indicating periodicity of roll-up, the first and the second pairings for SDP (see figure 1.3). We find that,  $v$  is high ( $1.3 - 1.6$ ) and  $\lambda$  is negative ( $-0.064 \leq \lambda \leq -0.032$  bpo) in the region between the first and the second pairing locations ( $120 \leq x/\theta_e \leq 170$ ); this is unexpected for a periodic flow state. Based upon earlier results (for SP) we infer that such  $v$  and  $\lambda$  estimates indicate noise-contaminated limit cycles.

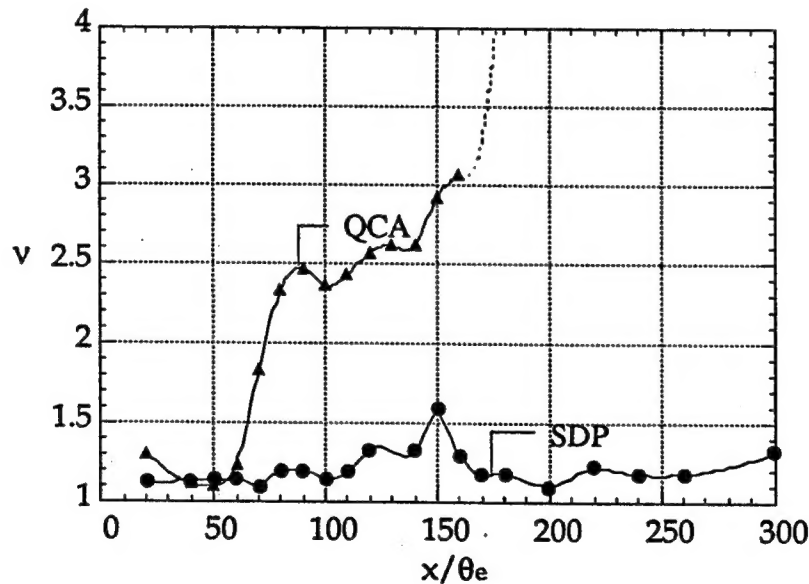


Fig. 1.3

Correlation dimensions for QCA show that  $v \approx 1.1-1.3$  ( $m = 4$ ) and  $\lambda \approx 0$  bpo for  $x/\theta_e \leq 60$ , due to periodic roll-up (see figure 1.3). However, for  $60 < x/\theta_e \leq 90$ ,  $v$  increases from 1.3 to 1.82, while  $\lambda$  is sizably negative ( $-0.089 \leq \lambda \leq -0.032$  bpo). The probe in this region detects the effects of periodic roll-up and modulated pairing, thus dimension calculations could yield an averaged  $v$  estimate ( $1 < v < 2$ ). Farther downstream, chaotic modulations of the second pairing are sensed, and consequently chaotic dynamics ( $v \approx 2.2-2.5$  and  $\lambda \approx 0.13-$



0.45 bpo) is found over a sizable flow region ( $90 \leq x/\theta_e \leq 150$ ). For  $x/\theta_e > 160$ , dimension estimates quickly exceed 3, scaling regions for  $v$  diminish and convergence is poor. This sudden increase in dimension corresponds to the onset of spatiotemporal dynamics inferred from decaying coherence and cross-bicoherence.

**Concluding remarks** By providing small amounts of forcing, we have triggered a *global instability* in the ML, allowing us to perform temporal analyses to infer dynamical states; however, this characterization is valid only in a flow domain where dynamics can be shown to be spatially coupled. We recommend the following approach: (i) use standard dynamical systems techniques to identify low-dimensional states (if any), and then (ii) identify dynamically significant phenomena and associated frequencies for these states, and estimate coherence and cross-bicoherence to determine the extent of spatial coupling in the flow. Such a combined approach (using dynamical systems and two-point spectral measures) can be used to describe large-scale dynamics in a wider class of open shear flows, such as boundary layers, jets and wakes.

The forced ML behaves as a *dynamically closed* flow in which spatially separated points are dynamically coupled via advecting rolled up and pairing vortices and feedback from these events. The *periodic* and low-dimensional *chaotic* temporal attractors, which occur in a wide region of control parameter space, were found to be global (evidenced by coherence and cross-bicoherence measurements). The periodic attractor SDP is found to be spatially coupled beyond the second pairing. For the chaotic attractor QCA, dynamics up to the first pairing is seen to be spatially well coupled. Farther downstream for the chaotic attractor, where the chaotic second pairing occurs, decaying coherence and cross-bicoherence indicate loss of spatial coupling, and is accompanied by a sudden increase in dimension. The loss of spatial coupling implies that the global dynamics in a flow domain that includes the second pairing (for the chaotic attractor) and the third pairing (for the periodic attractor) is disrupted. This does not necessarily imply that the second and third pairing dynamics are not feedback-driven anymore; *i.e.*, global dynamics could still be present but may be weak. In the absence of global dynamics, local dynamics alone dominate in different flow regions; *i.e.*, dynamics is spatiotemporal. We speculate that, for the chaotic attractor, the spatial disorder (*viz.* loss of spatial coupling) observed farther downstream is created by temporal chaos, and hence term the resulting downstream dynamics *spatiotemporal chaos*. However, a quantitative characterization of this behavior is lacking.

A quantitative description of spatiotemporal dynamics involves devising and implementing new measures (derived from signals sampled simultaneously in space-time) to provide sophisticated schemes/models for prediction and control of open shear flows. To do this, *multipoint* dynamical systems techniques must be developed from which spatiotemporal dimension and Lyapunov exponents can be extracted. These studies are currently being pursued and will be extended to noncanonical flows such as wall jets.

## 2. ODE models of spatially developing free shear flows

We are currently constructing a model using ordinary differential equations (coupled Landau equations) to describe multiple vortex pairings and feedback in a spatially developing mixing layer or jet:

$$\begin{aligned} A_x &= \alpha A - \gamma |A|^2 A - \mu |B|^2 A, \quad \text{and} \\ B_x &= \beta B - \delta |B|^2 B + \rho AB^* + \epsilon B(x-\chi), \end{aligned}$$

where  $A$  and  $B$  are the complex amplitudes of the fundamental (f) and subharmonic (s) waves respectively,  $\alpha$  and  $\beta$  are their respective linear growth rates,  $\gamma$  and  $\delta$  are their respective nonlinear saturation coefficients,  $\mu$  controls transfer of energy from f to s,  $\rho$  controls transfer from s to f, and  $\epsilon$  controls space-delayed feedback. By converting these complex waves into amplitudes and phases, three coupled ODEs result, with a total of 12 real coefficients (the real and imaginary parts of  $\alpha$ ,  $\beta$ ,  $\gamma$ ,  $\delta$ ,  $\mu$  and  $\rho$ , plus  $\epsilon$ , a tunable parameter). The most pressing problem is to express these coefficients in terms of the real control parameters of the system, *i.e.*, forcing frequency  $St_{\theta_e} = f_{ex}\theta_e/U_e$  and amplitude  $a_f = u'_f/U_e$ , where  $f_{ex}$  is the excitation frequency,  $\theta_e$  is the exit momentum thickness,  $U_e$  is the exit freestream velocity, and  $u'_f$  is the exit rms velocity perturbation at the forcing frequency. Preliminary estimates of the growth rates  $\alpha_r$  and saturation coefficients  $\gamma_r$  are shown in figure 2.1 as a function of  $St_{\theta_e}$ . These were estimated from amplitudes measured along the lip line of the mixing layer, and reproduce the growth and saturation of these modes quite well (figure 2.2).

Based on the success of the preliminary estimates, we are now extracting the coefficients from full 2D fields ( $u'(x,y)$ ) rather than along a single ray  $y = \text{constant}$ . Thus we can evaluate the spatial

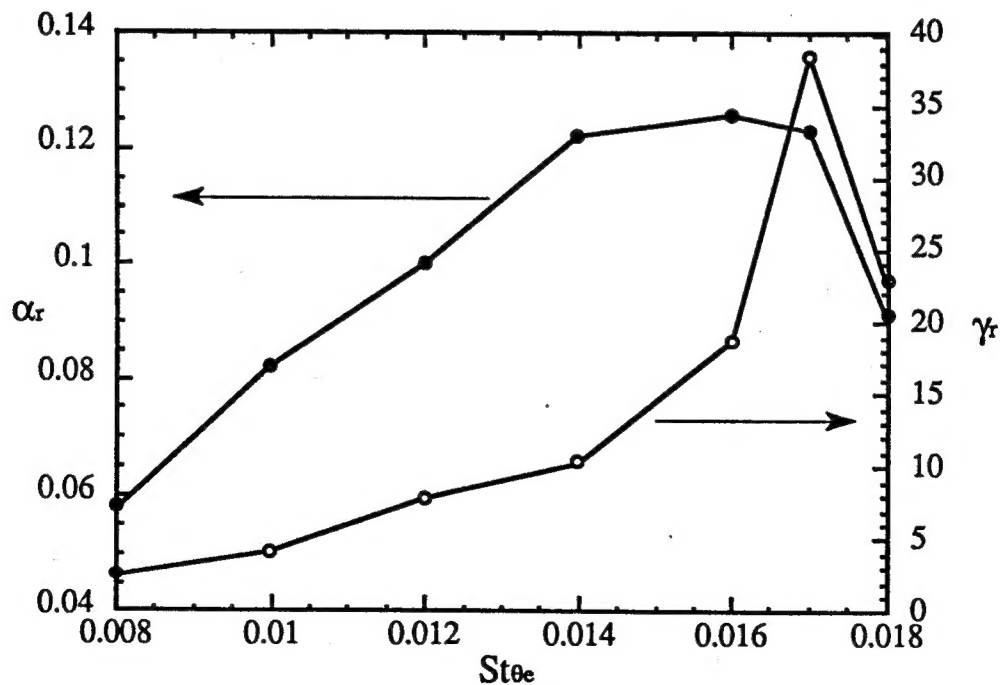


Figure 2.1: Landau coefficients as a function of forcing Strouhal number

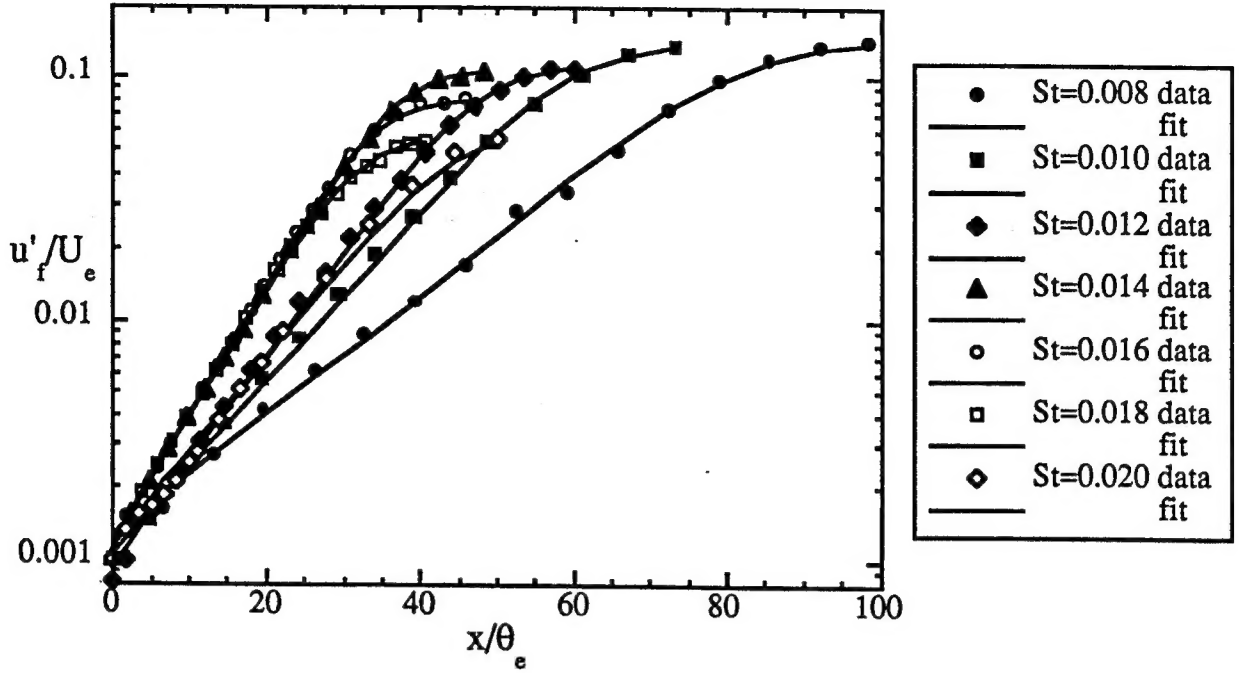


Figure 2.2: Agreement of experimental data with integration using Landau coefficients in fig. 2.1

evolution of *energy* within the eigenfunctions. However, phase estimation can become somewhat ambiguous since it changes in  $y$ ; we have devised a method to extract fundamental and subharmonic phases from integrals. We have measured 2D fields ( $u'_f$ ,  $u'_s$ ,  $\phi_f$  and  $\phi_s$ ) at 9 different  $St\theta_e$  in order to extract better values of the Landau coefficients, including the subharmonic resonance coefficients  $\rho_r$ ,  $\rho_i$ ,  $\mu_r$  and  $\mu_i$ . Examples of the  $u'$  fields are shown in figure 2.3 for  $St\theta_e = 0.012$ . The data are shown for only half (every other) of the  $x$  measurement stations.

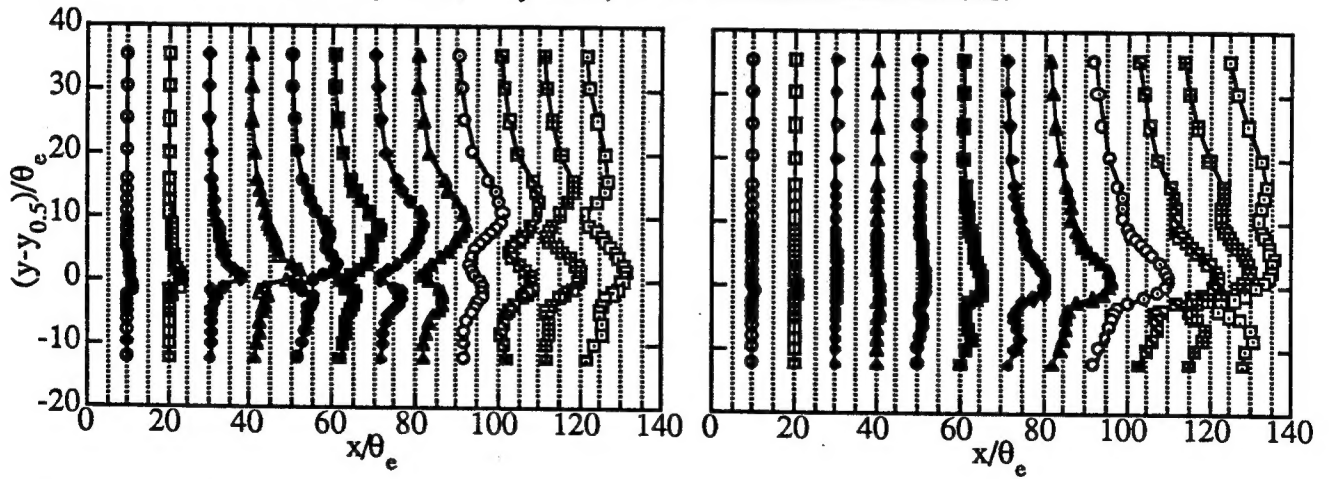


Figure 2.3: Fluctuation profiles at  $St\theta_e = 0.012$  for (a)  $u'_f/U_e$  and (b)  $u'_s/U_e$

Once coefficients are extracted, simulations of the dynamical system for different  $St\theta_e$  and  $a_f$  will be performed and compared with experiments.



### 3. Core dynamics and transition in a plane mixing layer

A new mechanism, termed *core dynamics instability* (CDI), has been identified which can promote an earlier mixing layer transition compared to transition dominated by longitudinal vortices ('ribs'). CDI is characterized by amplifying oscillations of core size nonuniformity and spanwise flow within pairing spanwise vortices ('rolls'), produced by a coupling of roll swirl and meridional flow, manifested by helical twisting and untwisting of roll vortex lines. We find that roll vorticity dynamics are dominated by CDI if ribs are not exceptionally strong; thus, CDI may govern small-scale transition for moderate-amplitude initial 3D disturbances, typical of practical situations. Results suggest that CDI is a new generic mechanism for transition to turbulence in shear flows.

CDI constitutes a new shear layer linear secondary instability, different from the longitudinal rib vortices prominent in experimental visualizations. CDI is an oscillatory temporal instability with frequency  $\sigma_i$ , so that along with exponential (linear) growth, its perturbation structure varies during the oscillation period. We find that the resulting CDI evolution is very similar to the oscillation of an axisymmetric vortex with initial axial core size variation (Melander & Hussain 1993).

A schematic of the vortex line and vortex surface evolution for inviscid, axisymmetric core dynamics is shown in figure 3.1 for a full oscillation period (note the distinction between vortex surfaces on which vortex lines lie and vorticity surfaces which can be crossed by vortex lines). The class of axisymmetric vortex surfaces consists simply of constant  $ru_\theta$  surfaces, where  $u_\theta$  is the azimuthal velocity around the vortex. Also shown are schematic streamlines of meridional flow (i.e.  $u_r$  and  $u_z$ ) in a plane through the vortex center. In the initial state (figure 3.1a), the diameter of this axisymmetric vortex surface (a representative core size) varies sinusoidally along the axis, with untwisted vortex lines (i.e.  $\omega_\theta=0$ ) and hence no initial meridional flow. Because the same circulation ( $\Gamma=2\pi ru_\theta$ ) is enclosed by a smaller core radius at  $\beta z=\pi$  than at  $\beta z=0$  – the symmetry planes hereinafter denoted by  $z_\pi$  and  $z_0$  respectively –  $u_\theta$  around this surface is higher at  $z_\pi$  than at  $z_0$ . Since the angular velocity is given by  $\dot{\theta}=d\theta/dt=u_\theta/r$ , both the smaller core radius and faster  $u_\theta$  at  $z_\pi$  cause faster angular rotation of this vortex surface at  $z_\pi$  relative to  $z_0$ . Thus, azimuthal vorticity  $\omega_\theta$  and hence cells of meridional flow are immediately generated as vortex lines on this and other vortex surfaces are twisted by this differential angular velocity, as reflected in figure 3.1(b). Recall that vortex lines are material and hence carry time history only in an inviscid flow.

In turn, the meridional flow cells induce two axisymmetric saddle flows: one with inward  $u_r$  and  $\omega_z$  stretching near the axis near  $z_0$ , and another with outward  $u_r$  and  $\omega_z$  compression near  $z_\pi$  (figure 3.1b). Since  $ru_\theta=\text{const}$  vortex surfaces are simply advected by meridional flow in an inviscid axisymmetric flow, the  $u_r$  induced by the meridional flow cells reduces the core size nonuniformity, eventually creating at one instant a virtually uniform vortex surface containing twisted vortex lines (figure 3.1c). At this point, the meridional flow cells continue to contract the vortex core at  $z_0$  and expand it at  $z_\pi$ , so that  $\dot{\theta}$  around the vortex surface becomes higher at  $z_0$  than at  $z_\pi$  (figure 3.1d). The differential  $\dot{\theta}$  now acts to untwist the vortex lines until a nearly untwisted state is reached (figure 3.1e), as in figure 3.1(a) except for a spanwise phase shift of the core size variation. Note that for nonlinear-amplitude perturbations at finite  $Re$ , the vortex lines became only approximately untwisted at this stage. In the remaining half-'period', the same dynamics cause the

vortex to return to nearly the initial state, as represented by figures 3.1(e)-(h).

For an isolated axisymmetric vortex, linear-amplitude core dynamics are neutrally stable in inviscid flow and damped by viscosity. In contrast, in the presence of a background shear, as in any free shear flow, core dynamics are linearly unstable. Therefore, for spanwise rolls in a mixing layer, the core dynamics represented by figure 3.1 grow exponentially in the linear regime, so that the degree of core nonuniformity and meridional flow strength increase with subsequent cycles.

We have found that CDI is most unstable when excited by the combination of 2D pairing and in-phase subharmonic oblique modes. This process is shown schematically in figure 3.2, with the 3D perturbation amplitude exaggerated for clarity. At rollup, subharmonic oblique modes cause opposite spanwise undulations of neighboring rolls (figure 3.2a), known as the helical pairing instability. Between rollup and pairing, these undulations amplify while, at the same time, pairs of rolls approach due to (nonlinear) 2D pairing growth (figure 3.2b). Once the rolls begin to coalesce (figure 3.2c), their opposite undulations create CDI-type meridional flow cells within the paired roll core (*cf.* figure 3.1), constituting the inception of *x-subharmonic CDI*, *i.e.*  $CDI_s$ .

To investigate the role of  $CDI_s$  in transition, we consider DNS of the finite-amplitude 3D evolution of the vortex interaction in figure 3.2. The evolution of spanwise vorticity  $\omega_z$  in the planes  $z_\pi$  and  $z_0$  shown in figure 3.3 provides a clear perception of the paired roll's core dynamics. To illustrate the strengthening and weakening of  $\omega_z$  in these planes, the same contour increment ( $0.2\Omega_0$ ) is used in all panels. In contrast to 2D pairing, the initially coalesced roll  $\omega_z$  in  $z_0$  ( $t = 21$ ) weakens and 'unpairs' by  $t = 27$ , due to the compression and outward ejection of roll fluid by the meridional flow cells. Between  $t = 30$  and  $t = 36$ , the cells reverse sign, causing the rolls to recombine and intensify in  $z_0$  to form a vortex sheet which undergoes secondary rollup by Kelvin-Helmholtz instability, reaching (by  $t = 36$ ) a peak  $\omega_z$  of  $4.4\Omega_0$  ( $\Omega_0$  is the initial peak vorticity).

In  $z_\pi$ , the rolls have slipped past each other without pairing by  $t = 21$  (figure 3.3a). Subsequently, the rolls coalesce ( $t = 24$ ), forming essentially a vortex sheet ( $t = 27$ ), which is strengthened by the extensional strain rate induced by the meridional flow cells. After this sheet rolls up between  $t = 27$  and  $t = 30$  into a single vortex in  $z_\pi$  (by Kelvin-Helmholtz instability), the cells reverse, causing the roll  $\omega_z$  to weaken. The compressive flow in this plane is so strong that a shell of  $\omega_z$  is formed around a bubble of nearly irrotational fluid ( $t > 33$ ). Expansion of this shell continues, forming an elongated and very thin sheath of  $\omega_z$  ( $t = 36$ ). The mechanism of sheath and bubble formation near  $z_\pi$  consists of a strong CDI-induced saddle flow centered at  $z_\pi$  which causes both compression and outward ejection of near-axis  $\omega_z$ .

We have found that a useful indicator of transition is the development of strong opposite-to-mean  $+\omega_z$ , which reflects a qualitative change in the vortex line geometry – from vortex lines which all run in the  $-z$  direction before transition to the appearance of folded vortex lines with S-shaped kinks which locally run opposite to the mean vorticity direction (*i.e.*  $+z$ ). To determine where this opposite-signed  $\omega_z$  develops for  $CDI_s$ , we show in figure 3.4(a) a bundle of vortex lines centered in the roll core in  $z_{\pi/2}$  along with the corresponding isosurface plot in figure 3.4(c) of  $|\omega|$  (grayscale) overlaid by  $+\omega_z$  (crosshatch) at  $t=37.5$  (the time of maximum  $+\omega_z$ ). Viewed together, figures 3.4(a),(c) illustrate that  $+\omega_z$  is localized around the vortex sheath near  $z_\pi$  and results

from folded vortex lines which flare outward intensely here. Note that between  $z_0$  and  $z_{\pi/2}$ , the roll's vortex line and  $|\omega|$  distributions are those of a laminar, albeit strongly 3D, flow. Contour plots of  $\omega_z$  near  $z_{\pi}$  (in the  $z$  plane containing the maximum  $+\omega_z$ ) at  $t=33$  and  $37.5$  in figures 3.5(a,b) respectively clearly illustrate the internal intermittency resulting from this  $+\omega_z$  development. Specifically, layers of  $+\omega_z$  first appear within the roll ( $t=33$ ), followed by development of intermingled regions of high-valued, fine-scale  $-\omega_z$  and  $+\omega_z$  within the roll ( $t=37.5$ ). This suggests that strong core dynamics have initiated localized transition near the vortex sheath.

To ensure that this is in fact a turbulent transition, we increased the initial 3D energy of the  $CDI_s$  mode to  $E_{3D}(0)=E_{2D}(0)$ , which is twice the amplitude of the case of figures 3.3, 3.4(a,c), and 3.5(a,b). In this higher amplitude case, similar core dynamics occur, and the locally entangled vortex lines and fine-scale vorticity in figures 3.4(b),(d) indicate transition near  $z_{\pi}$ . The  $\omega_z$  distribution near  $z_{\pi}$  in figure 3.5(c) shows strong internal intermittency and ensures that the fine scales in figure 3.4(d) are not numerical noise.

During transition for the  $E_{3D}(0)=0.5E_{2D}(0)$  case, the volume-integrated energy and dissipation spectra increase as much as 3 orders of magnitude at higher wavenumbers ( $|k| \sim 50$ ) between  $t = 9-37.5$ , as illustrated in figure 3.6(a). Note that the two decade fall-off of the dissipation spectra indicates adequate numerical resolution (for  $128^3$  grid points). An interesting aspect of the spectral evolution is the fact that most of the small-scale generation occurs by  $t \sim 33$ , even though little intermittency (*i.e.* spatial patchiness of vorticity) has been generated by this time (see figure 3.5a). This indicates that the growth of high wavenumbers is not accompanied by internal intermittency. That is, sharp vorticity gradients reflected at high wavenumbers do not necessarily imply the presence of a granular 3D vorticity distribution, characteristic of intermittency. Therefore, in this case, cascade enhancement is not caused by the appearance of roll intermittency, but rather by strong core dynamics. Once small-scale vorticity is generated, vortex lines are quickly disrupted by locally intense vorticity, producing internal intermittency but only slight additional small-scale energy (*cf.*  $t = 33$  and  $t = 37.5$  spectra in figure 3.6a). In this sense, internal intermittency appears to be more a consequence of, and not synonymous with, nor a cause of, growth of high wavenumbers. Thus, accelerated small-scale and internal intermittency generation indicate the onset of localized transition between the first and second pairings due to nonlinear evolution of a single  $CDI_s$  mode, without either pairing suppression or artificially high initial 3D disturbance levels.

This  $CDI_s$  based transition scenario would be only of theoretical interest if it were seriously disrupted by the presence of ribs, which are frequently observed in laboratory experiments. To investigate the effect of this interaction, simulations were performed of the simultaneous evolution (through pairing) of  $CDI_s$  and ribs excited in the braid region between rolls. We found that  $CDI_s$  grows alongside ribs, with the roll dynamics dominated by  $CDI_s$  and ribs prominent in the braid. We emphasize that our analysis of the vorticity field evolution unmistakably shows that  $CDI_s$  is *not* reliant upon special flow symmetries and can occur vigorously side-by-side with ribs. Combined with our observation that  $CDI_s$  is the only secondary instability which produces transition from moderate amplitude 3D disturbances ( $E_{3D}(0) \sim E_{2D}(0)$ ), these results are strong evidence that  $CDI_s$  may play a prominent role in shear layer transition, provided that ribs are not artificially strong.

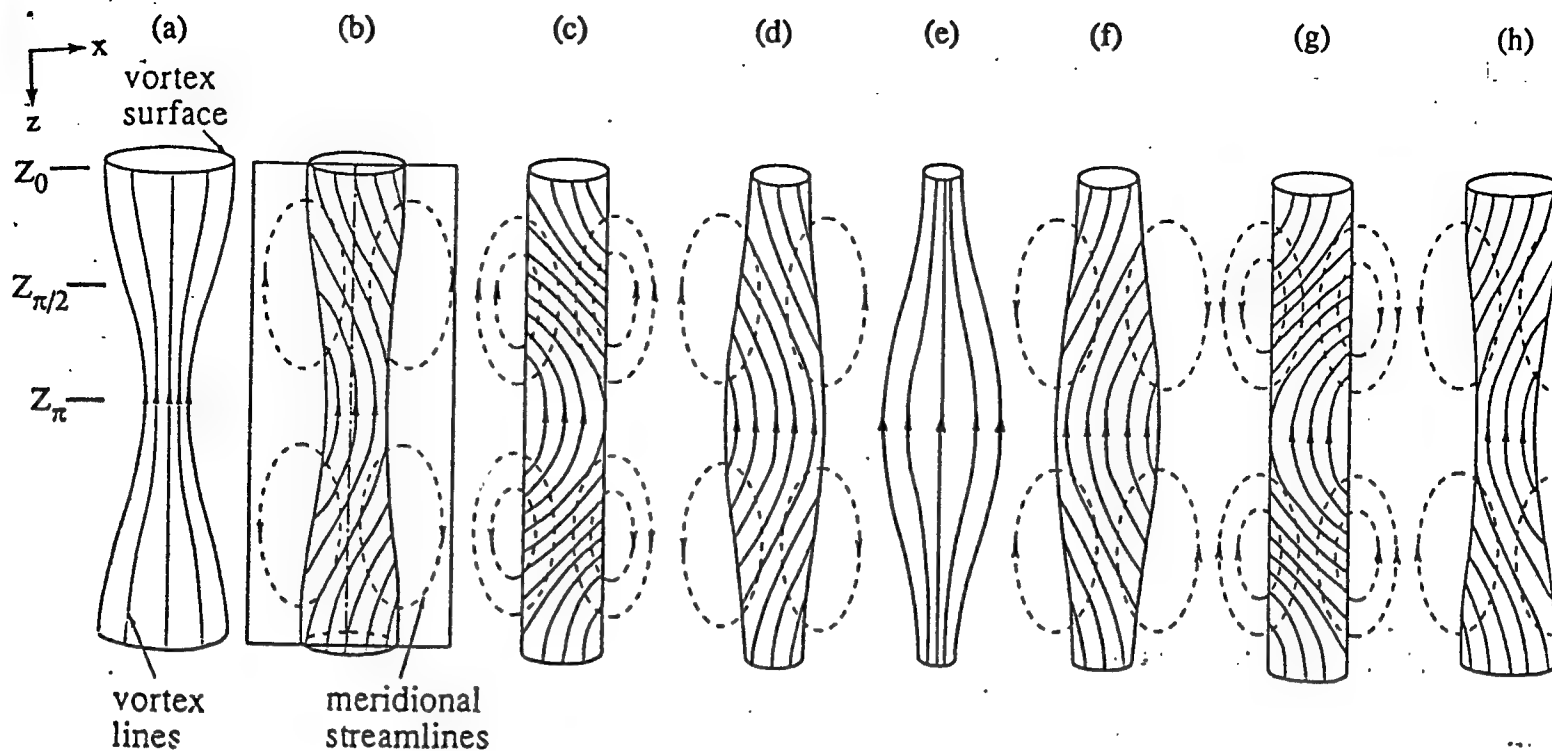


Figure 3.1 Schematic of one oscillation period for axisymmetric core dynamics at a finite amplitude. The vortex lines shown lie on one axisymmetric vortex surface, and the dashed lines represent streamlines of the meridional flow, induced by helically twisted vortex lines.

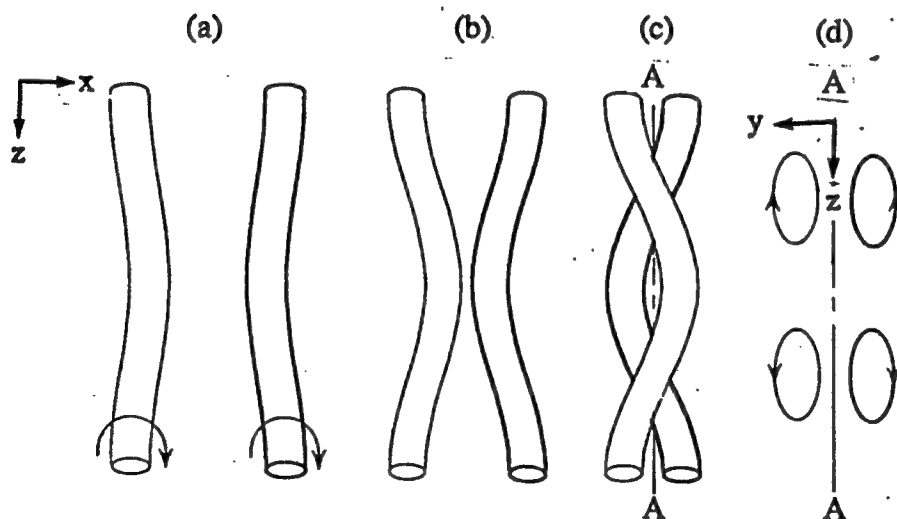


Figure 3.2 Schematic of  $CDI_s$  excitation by the combination of roll pairing and subharmonic oblique modes.

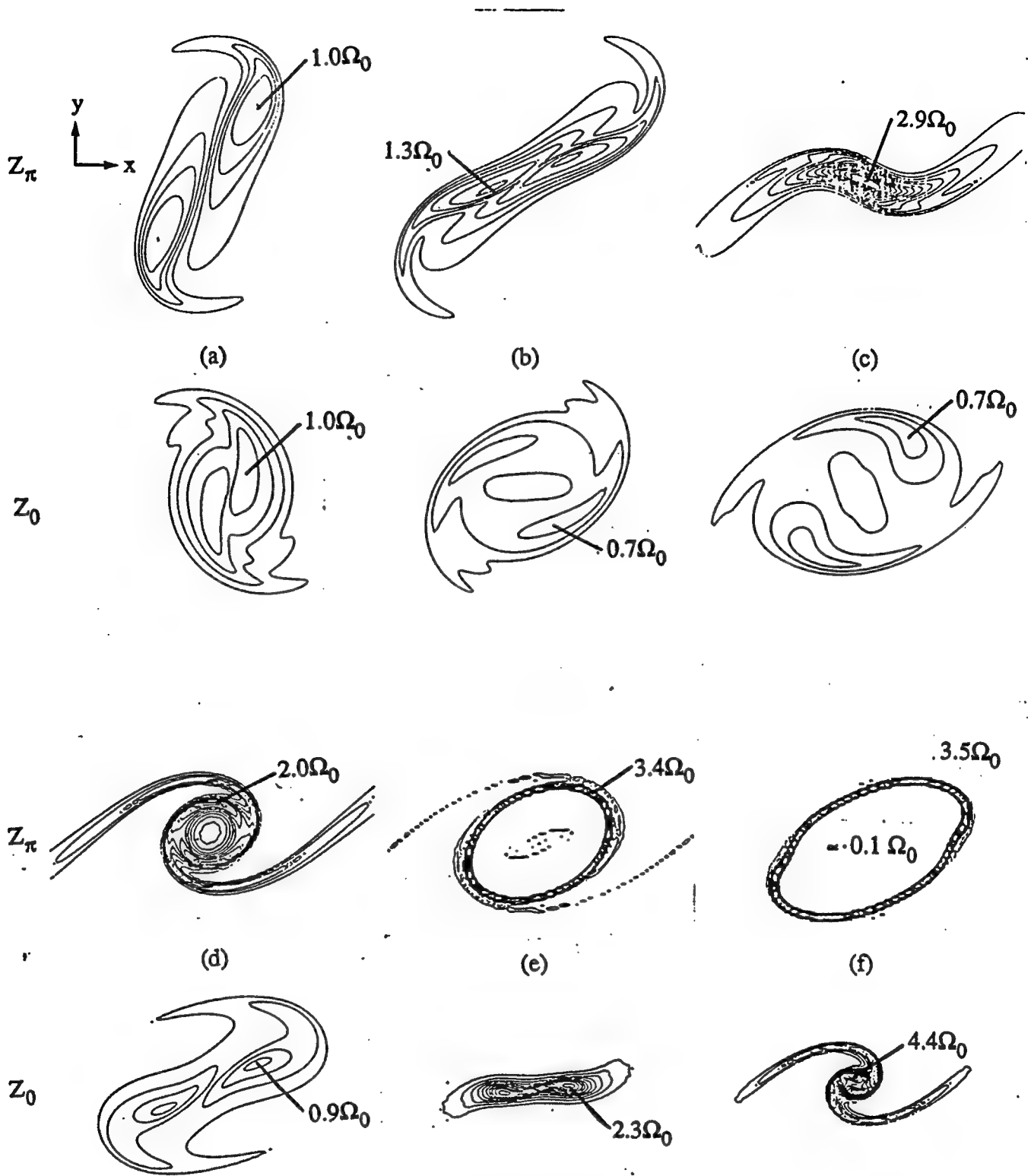


Figure 3.3 Evolution of the  $\omega_z$  distribution in  $z_\pi$  and  $z_0$  for  $CDI_s$  at times (a)  $t=21$ , (b)  $t=24$ , (c)  $t=27$ , (d)  $t=30$ , (e)  $t=33$ , and (f)  $t=36$ . The contour increment is  $0.2\Omega_0$  starting with this value, with the peak values indicated.

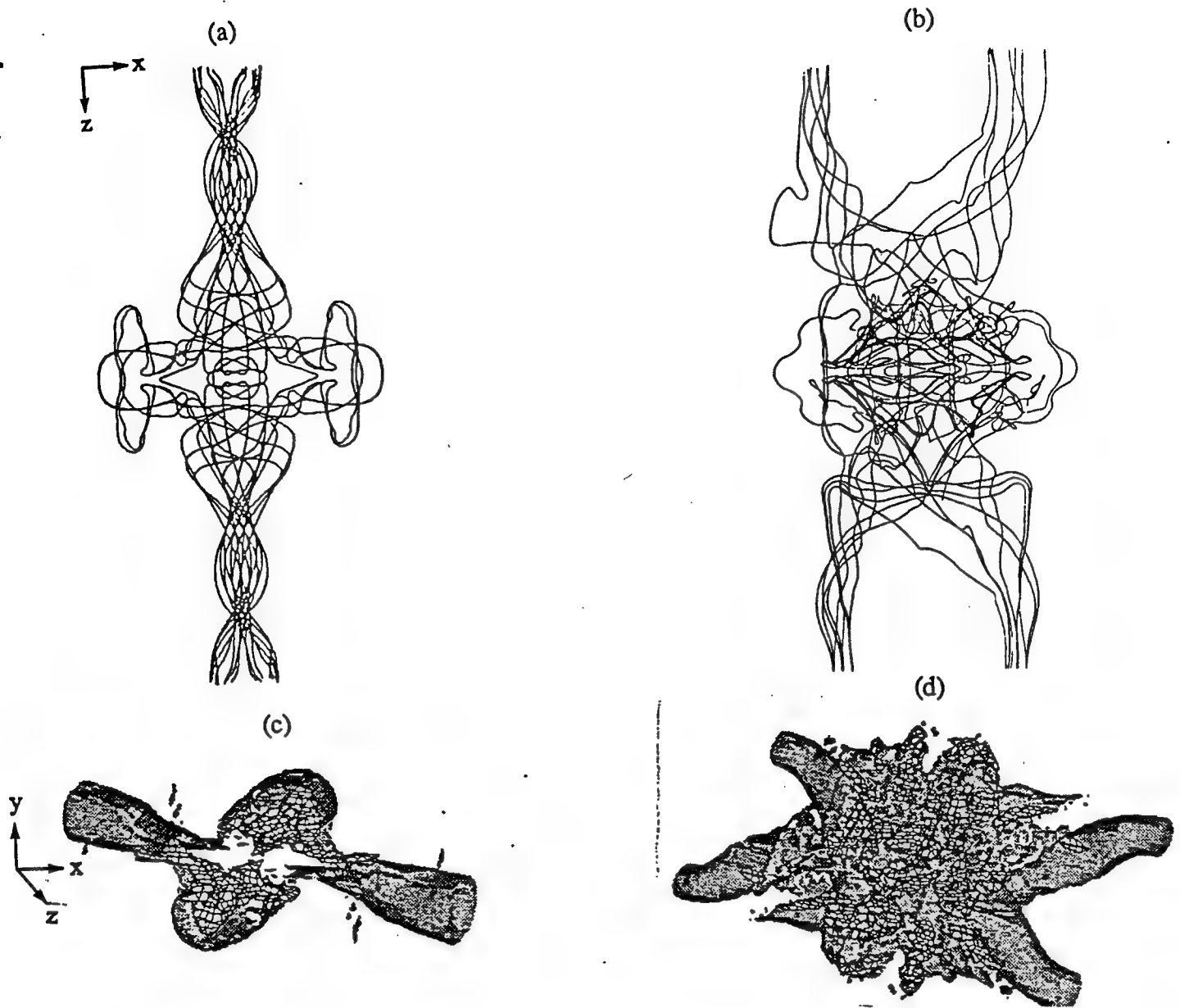


Figure 3.4 Onset of transition for  $CDI_s 0.5$ , reflected by roll vortex lines in (a,b) and  $|\omega|$  isosurface overlaid with cross-hatched surfaces of opposite-to-mean  $+\omega_z$  in (c,d). The initial 3D perturbation energy is  $E_{3D}(0)=0.5E_{2D}(0)$  in (a,c) and  $E_{3D}(0)=E_{2D}(0)$  in (b,d).

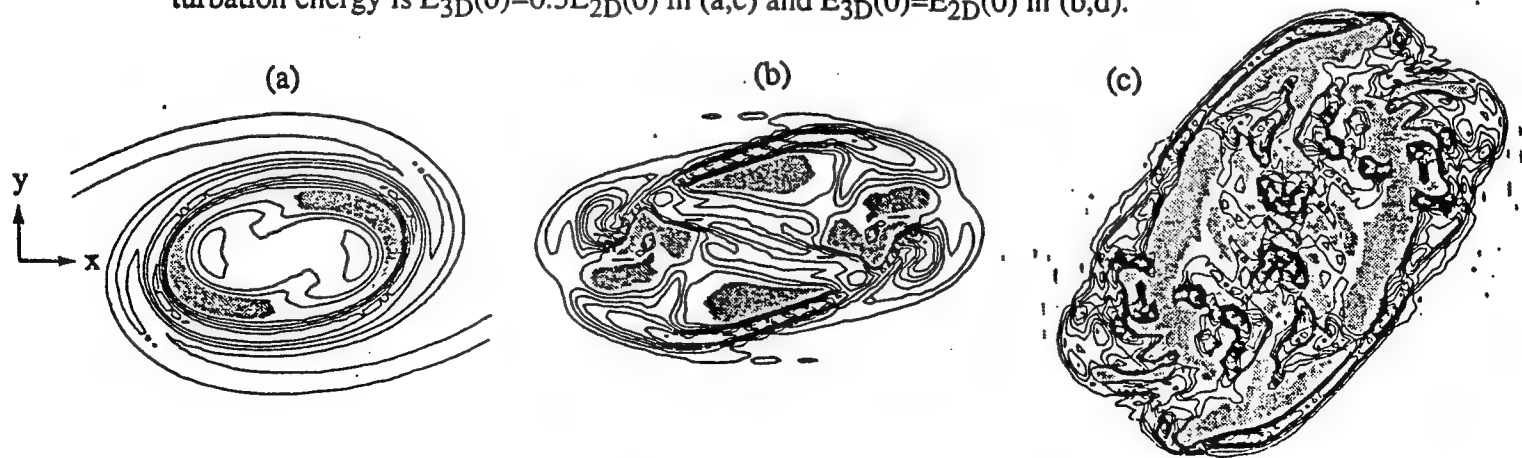


Figure 3.5 Development of internal intermittency, illustrated by the  $\omega_z$  distribution in an  $(x,y)$  plane near  $z_\pi$  for  $CDI_s 0.5$ . The initial amplitudes are:  $E_{3D}(0)=0.5E_{2D}(0)$  at (a)  $t=33$  and (b)  $t=37.5$  and (c)  $E_{3D}(0)=E_{2D}(0)$  at  $t=39$ .



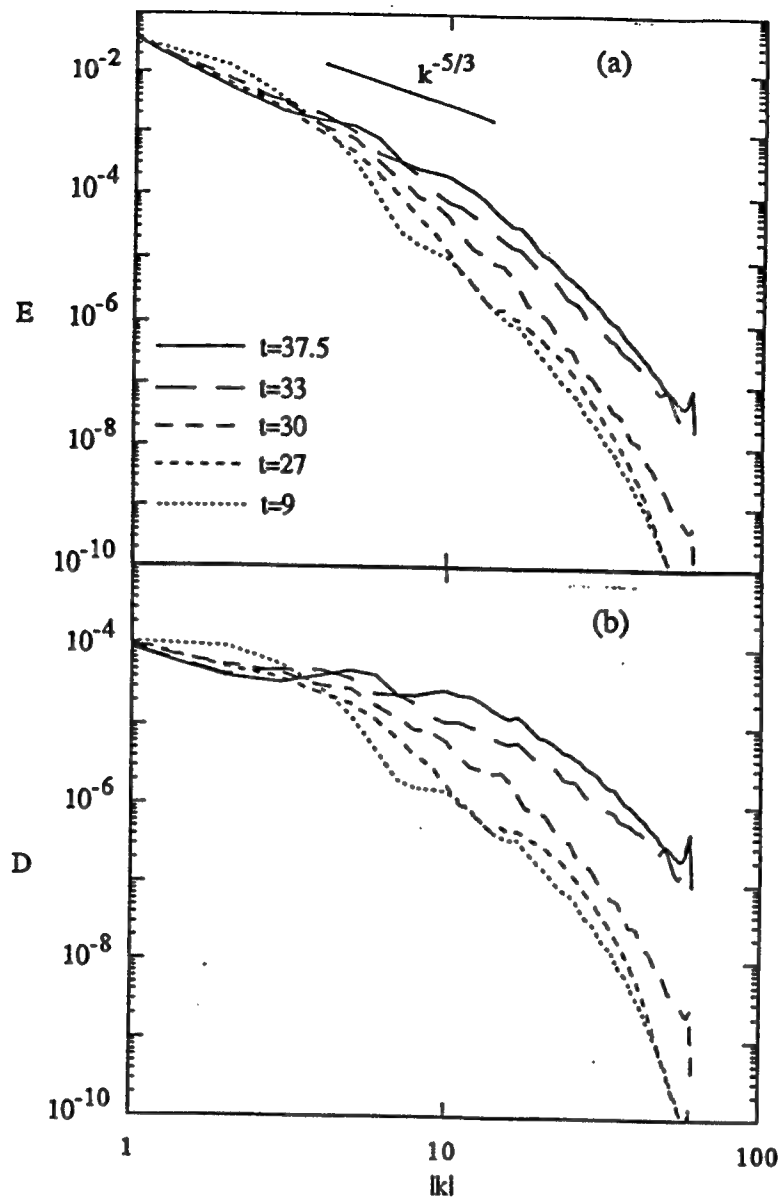


Figure 3.6 Development of (a) energy and (b) dissipation spectra for  $CDI_s$ .

## 4. Vorticity and helicity statistics in a circular jet

**Vorticity statistics** Despite the importance of vorticity measurements for turbulent flows, until recently most experiments have been based on the measurement of either one or two velocity components and the use of various simplifying assumptions to calculate the dynamical quantities in the flow. This has been primarily due the difficulty in measuring all three velocity components with sufficient accuracy, to enable the calculation of velocity derivatives with adequate resolution, to compute the vorticity vector. Consequently, velocity based measures, namely the transport and production of turbulent kinetic energy, its diffusion and dissipation have been used to describe the flow.

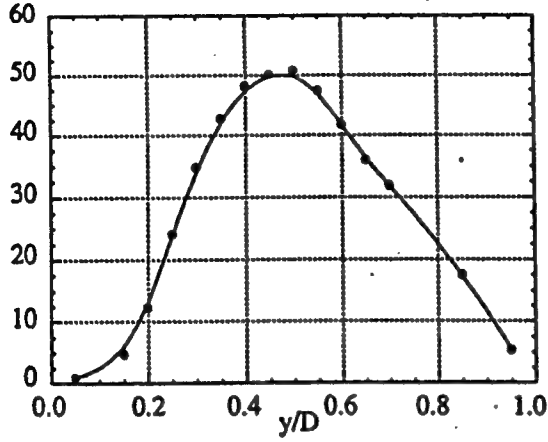
Only recent innovations in multi-sensor probes have made a direct measurement of vorticity components possible. Vukoslavčević *et al.*(1989) developed a multi-sensor hotwire probe to directly measure the vorticity in turbulent flows. Subsequently several vorticity based studies have been made in various flows (Balint *et al.*(1991) in a turbulent boundary layer, Balint & Wallace (1988) in a two-stream mixing layer, etc. ). Here we report on our studies of vorticity statistics and balance of turbulent enstrophy in a circular jet using a nine-sensor vorticity probe.

**Mean & r.m.s. values** The measured vorticity mean values indicate that the spanwise vorticity component,  $\Omega_z$ , is the only measureably non-zero mean component. Its variation across the mixing layer is shown in Fig. 4.1(a). However, the r.m.s. profiles in Fig. 4.1(b) show appreciable values of both transverse and spanwise components.

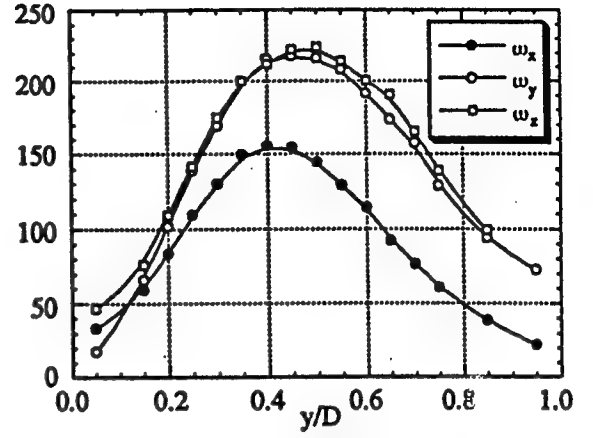
This presence of significant transverse component,  $\omega_y$ , implies that the predominantly ring like structure of the jet is getting distorted and is developing 'kinks' in the radial direction. The streamwise fluctuation,  $\omega_x$ , is still significantly lower than the other two components indicating that the flow is yet to develop statistically dominant streamwise structures. The low r.m.s. values of streamwise component do not signify their absence but that the duration of time over which they were present in the flow is small as compared to the time over which averages were calculated.

**Skewness & flatness factors** Figure 4.2(a) shows the skewness factors of the three vorticity components. The skewness for the streamwise and the transverse components is negligible across most of the mixing layer.  $\omega_z$  has positive skewness values, indicative of predominant spanwise fluctuations due to the large scale structures in the flow. The large positive skewness near the centerline is likely due to contribution from sharp positive spikes in the vorticity signal caused by the passage of the structures.

Figure 4.2(b) shows the distribution of the flatness factor across the flow. To show deviation from Gaussian distribution, a value of 3 has been subtracted. Flatness factor values are nominally positive and increase toward the edges of the mixing layer indicating the increased intermittent nature of the shear layer. The high positive values near the extremes of the jet in both skewness and kurtosis calculations are probably due to lack of convergence of the data as the values were found to vary considerably with the length of the data used in the calculations.

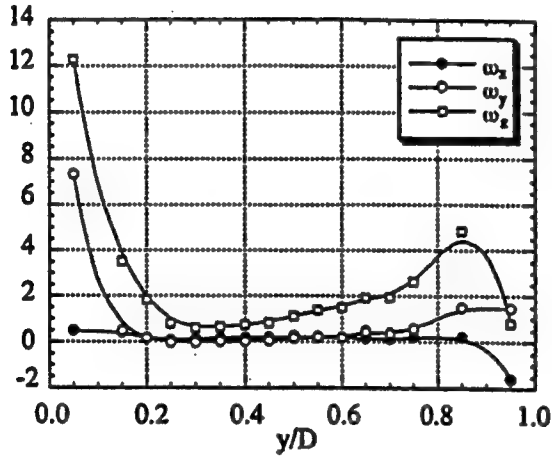


(a)

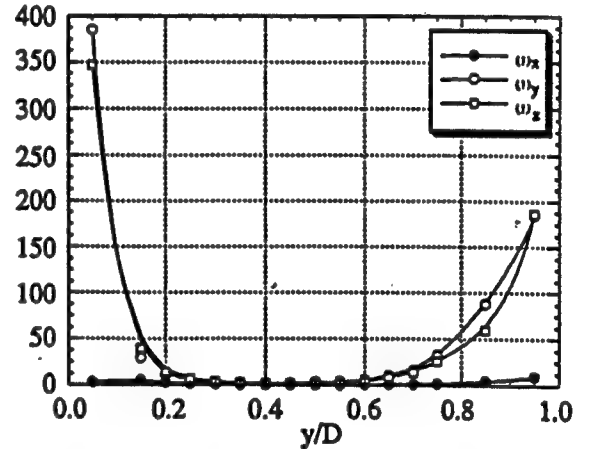


(b)

FIGURE 1. (a) Variation of mean spanwise vorticity across the mixing layer and (b) Profiles of the r.m.s. values of the three vorticity components.



(a)



(b)

FIGURE 2. Transverse variation of (a) Skewness of the three vorticity components across the mixing layer; and (b) Kurtosis of the three vorticity components across the mixing layer. Note that a value of 3.0 for a Gaussian random variable has been subtracted from Kurtosis values at all transverse locations.

**Enstrophy balance across the mixing layer** The balance equation for the transport of fluctuating enstrophy is given by

$$\underbrace{U_j \partial_j \left( \frac{1}{2} \overline{\omega_i \omega_i} \right)}_{L1} = \underbrace{-\overline{\omega_i u_j} \frac{\partial \Omega_i}{\partial x_j}}_{R1} - \underbrace{\frac{1}{2} \frac{\partial}{\partial x_j} (\overline{u_j \omega_i \omega_i})}_{R2} + \underbrace{\Omega_j \overline{\omega_i s_{ij}}}_{R3} + \underbrace{\overline{\omega_i \omega_j} S_{ij}}_{R4}$$

$$+ \underbrace{\overline{\omega_i \omega_j s_{ij}}}_{R5} + \underbrace{\nu \frac{\partial^2}{\partial x_j \partial x_j} \left( \frac{1}{2} \overline{\omega_i \omega_i} \right)}_{R6} - \underbrace{\nu \left( \frac{\partial \omega_i}{\partial x_j} \right) \left( \frac{\partial \omega_i}{\partial x_j} \right)}_{R7}. \quad (4.1)$$

The interpretation of the above terms are given in Tennekes & Lumley (1987). Figure 4.3 shows the distribution of the values of the terms in the equation for turbulent enstrophy for locations across the mixing layer. The major contribution to the turbulent enstrophy in the flow is through the production caused by the mean and the fluctuating strain rates which is transported away by the mean and fluctuating strain rates (terms R2 and L1). The large contribution due to the production term R5 is expected since the fluctuating strain rates are much larger than the mean strain rates and the vorticity fluctuations are also greater than the mean flow vorticity. The dissipation term cannot be measured with the probe and is obtained as residual balance of the other terms in the equation.

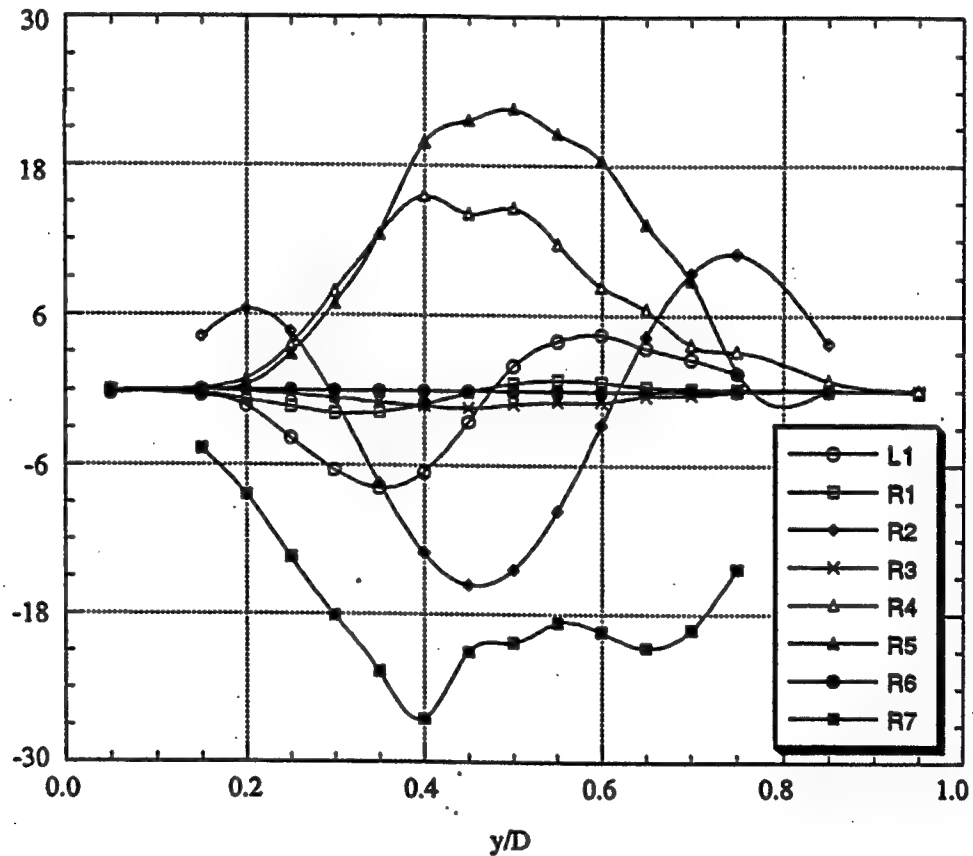


FIGURE 3. Budget of the enstrophy fluctuations across the mixing layer. Individual terms are explained in the text.

### Helicity in turbulent flows

The ability to directly measure vorticity in a turbulent flow enables us to study an

important invariant of fluid flows - its helicity. The concept of helicity,  $H = \int h dV$  (where  $h = \mathbf{u} \cdot \boldsymbol{\omega}$  is the helicity density) was introduced to fluid mechanics by Moffatt (1975) from an analogy in magnetic fields. He showed that  $H$  is a property of the topology of vortex lines in a space bounded by a closed vortex surface and a measure of the degree of knottedness in that space. Therefore, helicity conservation is important as it characterises a topology-invariant evolution of nonlinear inviscid dynamics.

Calculations and analysis based in local  $h$  values have been controversial. Based on the analysis in Moffatt (1969), Tsinober & Levich (1983) and Moffatt (1985) suggested that large scale CS in turbulent flows are characterized by extreme values of relative helicity density ( $h_r = h/|h|$ ) and dissipation is concentrated in sheets surrounding these CS. Rogers & Moin (1987) in numerical studies of channel flows and Balint *et al.* (1992) in experimental studies of turbulent boundary layers found no correlation between the relative helicity density and dissipation of turbulent kinetic energy.

However, a judicious use of  $h$  analysis can provide some insight to the dynamics of turbulent flows. While  $\mathbf{u} \cdot \boldsymbol{\omega}$  is not Galilean invariant, its turbulent part,  $\mathbf{u}' \cdot \boldsymbol{\omega}'$  is, and we have the following algebraic expression

$$|\mathbf{u}'|^2 |\boldsymbol{\omega}'|^2 = (\mathbf{u}' \times \boldsymbol{\omega}')^2 + (\mathbf{u}' \cdot \boldsymbol{\omega}')^2. \quad (4.2)$$

In terms of time-averaged quantities,  $\langle \mathbf{u}' \times \boldsymbol{\omega}' \rangle$  can be represented as

$$\langle \mathbf{u}' \times \boldsymbol{\omega}' \rangle = \langle \nabla \left( \frac{1}{2} \mathbf{u}' \cdot \mathbf{u}' \right) \rangle + \nabla \cdot \tilde{\mathbf{R}}, \quad (4.3)$$

where  $\tilde{\mathbf{R}}$  is the Reynolds stress tensor. Hence, the effects of helicity appears as gradient of the Reynolds stress in the flow. This correlation between the flow Reynolds stresses and helicity fluctuations is also evident in a study of the balance of helicity transport across the mixing layer.

**Helicity Transport Equation** The equation for the transport of flow helicity can be derived by taking the inner product of the momentum equation with vorticity and the inner product of the vorticity equation with velocity and adding the corresponding left and right hand sides. The balance equation for the transport of fluctuating helicity is given by

$$\begin{aligned} \underbrace{U_j \frac{\partial}{\partial x_j} (\overline{u_i \omega_i})}_{L1} + \underbrace{u_j \frac{\partial}{\partial x_j} (\overline{u_i \omega_i})}_{L2} = & \underbrace{-\overline{u_i u_j} \frac{\partial \Omega_i}{\partial x_j}}_{R1} + \underbrace{(\overline{\omega_j u_i} - \overline{u_j \omega_i}) S_{ij}}_{R2} \\ & + \underbrace{\Omega_j \overline{u_i s_{ij}}}_{R3} - \underbrace{\frac{1}{\rho} \overline{\omega_i \frac{\partial p}{\partial x_i}}}_{R4} + \underbrace{\overline{\omega_j u_i s_{ij}}}_{R5} \\ & + \underbrace{\nu \frac{\partial^2}{\partial x_j \partial x_j} (\overline{u_i \omega_i})}_{R6} - \underbrace{2\nu \left( \frac{\partial u_i}{\partial x_j} \right) \left( \frac{\partial \omega_i}{\partial x_j} \right)}_{R7}. \end{aligned} \quad (4.4)$$

The terms in the above equation can be interpreted as follows. The two terms on the left-hand side are the advection of the fluctuating helicity by the mean velocity and the velocity fluctuations respectively. The first term on the right-hand side is the gradient production of helicity due to the Reynolds stresses. The second term is the transport of turbulent helicity due to the mean strain rate. The third and fifth terms on the right-hand side are the mixed production terms due to stretching by the mean and fluctuating strain rates, while fourth is the transport of helicity fluctuations due to the pressure gradient. The last two terms are the viscous diffusion and dissipation of helicity fluctuations.

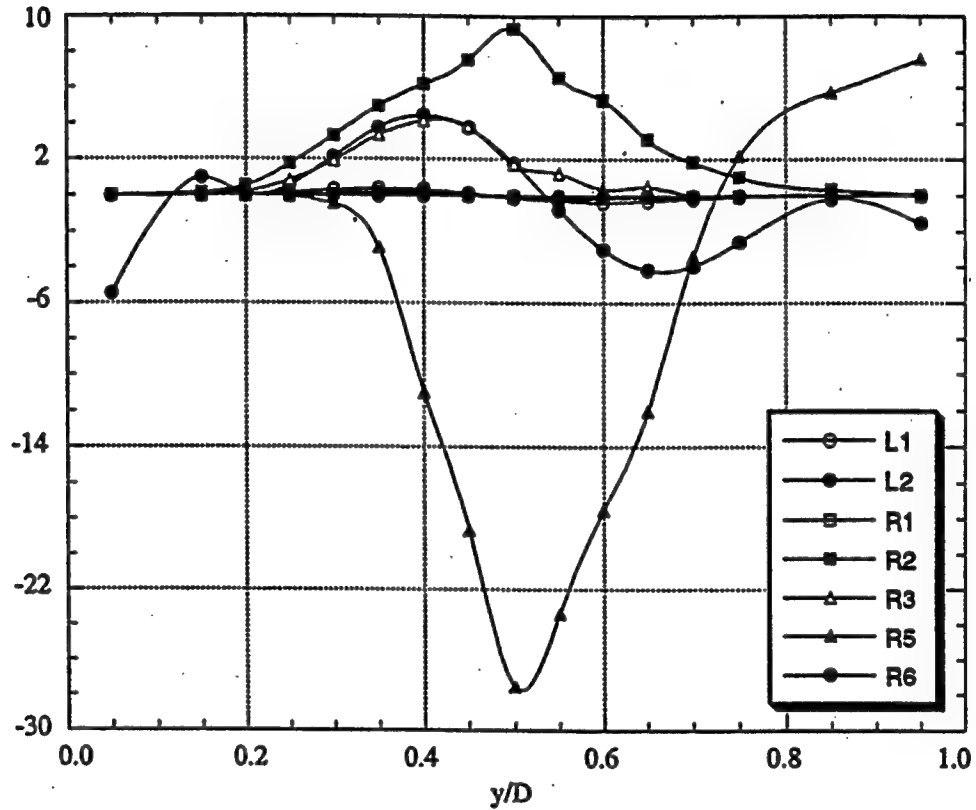


FIGURE 4. Budget of the fluctuating helicity across the mixing layer. Individual terms are explained in the text.

Figure 4.4 shows the distribution of these terms across the mixing layer. As can be seen, R5 is the most dominant term, which supports the order of magnitude estimation made above and is the major source of production of helicity fluctuation in the flow. The terms L2, R2 and R3 are considerably lower in magnitude than R5 as predicted by the estimation above. The production of fluctuating vorticity by the fluctuating strain rates is balanced across the mixing layer by the transport of the fluctuating helicity by R2 and the production of opposite signed fluctuations by R3. Terms R4 and R7 cannot be computed and, hence, have not been plotted.



*Helicity and Entrainment* Hunt & Hussain (1991) hypothesized a possible relationship between helicity fluctuations and the entrainment at a boundary between rotational and irrotational motions, which occur in jets, wakes, mixing layers, etc. . They proposed that if the interface between turbulent-nonturbulent fluid is to move outward into the irrotational fluid and entrain ambient fluid, helicity density fluctuations must be small. This hypothesis is important in view of the fact that there is no direct measure of the entrainment at an interface, a validation of the hypothesis would help correlate the regions where most entrainment occurs based on the local values of random helicity density fluctuations.

As vorticity is solenoidal, at the surface of a CS lying between vortical and irrotational flow, the normal component of vorticity must be zero, i.e. ,  $\omega \cdot \hat{n} = 0$ . If the vorticity vector is decomposed into the vorticity associated with the large scale structure,  $\omega_c$ , and the incoherent field,  $\omega_{rc}$ , then  $\omega_c \cdot \hat{n} = 0$  and  $\omega_{rc} \cdot \hat{n} = 0$ . If ambient fluid is being entrained at the interface, then it means that the surface is moving outward relative to the local large scale convection velocity,  $u_c$ . This implies  $u_{rc} \cdot \hat{n} \neq 0$ , where  $u_{rc}$  is the incoherent velocity vector. Therefore, near the interface between turbulent and irrotational fluid, where the entrainment is high,  $|u_{rc} \cdot \omega_{rc}|$  is small compared to  $(u_{rc}^2/\ell)$  where  $\ell$  is the length scale of the incoherent velocity fluctuations and  $u_{rc}^2 = u_{rc}^2$ .

As entrainment rate cannot be measured experimentally, a validation of this hypothesis will provide a useful measure of studying regions where ambient fluid is being entrained. For a given vorticity time-series, this implies studying the pdf of the relative helicity density conditioned on the magnitude of the vorticity at any instant. A threshold is set on the vorticity value to demarcate the interface between turbulent and irrotational fluid, and a probability distribution of the relative turbulent helicity is obtained.

This analysis has been carried out for the vorticity time series at various transverse locations. Figure 4.5 shows the fluctuating relative helicity density pdf conditioned on a range of vorticity (namely  $\Omega_z \pm \sigma$ , where  $\sigma$  is the standard deviation of  $\omega_z$ ). As can be seen from the figure, irrespective of the transverse location, the pdf is skewed towards zero values of helicity. The skewness is more distinct away from the center of the mixing layer, which can be explained because the flow is more intermittent in those regions and therefore, there are more regions of turbulent-nonturbulent interface in the flow.

## References

- BALINT, J. -L., WALLACE, J. M. & VUKOSLAVČEVIĆ, P. 1991 The velocity and vorticity vector fields of a turbulent boundary layer. Part 2. Statistical properties *J. Fluid Mech.* **228**, 53.
- HUNT, J. C. R. & HUSSAIN, F. 1991 A note on velocity, vorticity and helicity of inviscid fluid elements. *J. Fluid Mech.* **229**, 569.
- HUSSAIN, A. K. M. F. 1986 Coherent structures and turbulence. *J. Fluid Mech.* **173**, 303.
- MOFFATT, H. K. 1969 The degree of knottedness of tangled vortex lines. *J. Fluid Mech.* **35**, 117.
- MOFFATT, H. K. 1985 Magnetostatic equilibria and analogous euler flows of arbitrarily complex topology. *J. Fluid Mech.* **159**, 359.
- ROGERS, M. M., & MOIN, P. 1987 Helicity fluctuations in incompressible turbulent flows. *Phys. Fluids* **30** (9), 2662.

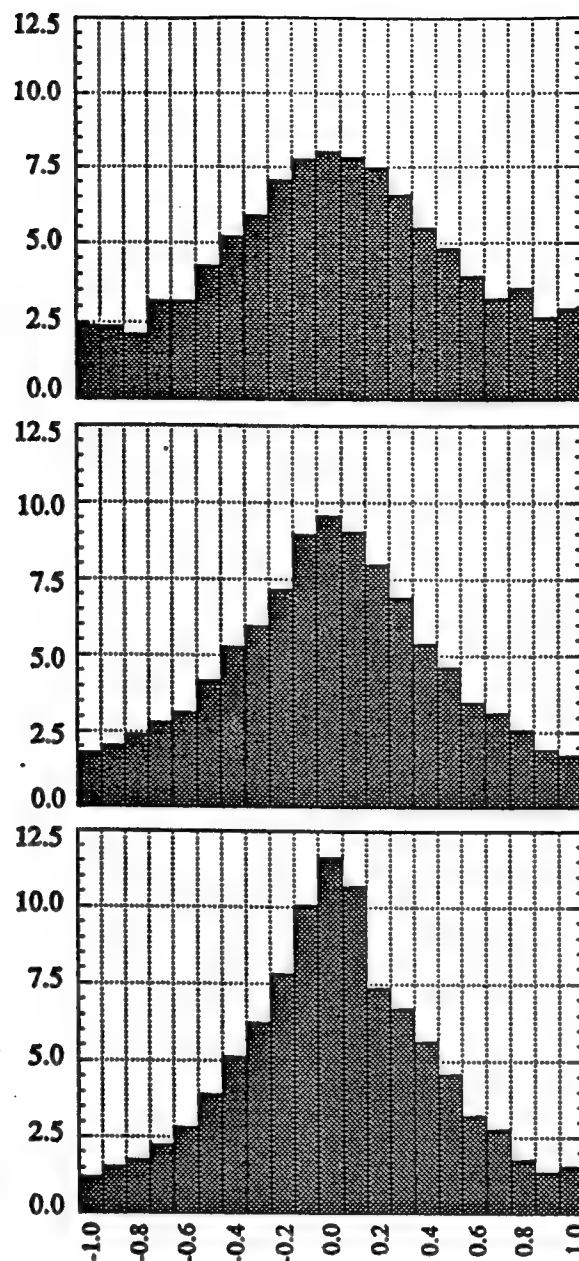


FIGURE 5. Histograms of the number of occurrences of relative helicity density values in various intervals between  $-1.0$  and  $1.0$ . Histograms at (a) the inner edge of the mixing layer; (b) the lip-line of the jet; and (c) the outer edge of the mixing layer.

TENNEKES, H. & LUMLEY, J. L. 1972 A First Course in Turbulence. The MIT Press.

TSINOBER, A. & LEVICH, E. 1983 On the helical nature of three-dimensional coherent structures in turbulent flows. *Phys. Lett.* 99A (6,7), 321.

VUKOSLAVČEVIĆ, P., BALINT, J. -L. & WALLACE, J. M. 1989 A multi-sensor hot-wire Probe to measure vorticity and velocity in turbulent flows. *J. Fluids Engr. (ASME)* 111 (2), 220.

## 5. New approaches to identify sources of jet noise

Noise generated by nearly axisymmetric vortex pairing in an excited low Mach number jet was studied experimentally as a prototypical jet noise source using a three-dimensional microphone array. The measured time-dependent sound field was decomposed into its multipole components using general linear regression techniques. Although the vortex interactions were very nearly axisymmetric and thus a nearly axisymmetric lateral quadrupole sound field was expected, the sound field was found to have large departures from axisymmetry. This acoustic sensitivity to symmetry breaking in the vorticity field was also shown in calculations using numerical vortex models and vortex sound theory. The directivity of the far-field sound gets smeared out in the time averaged data due to the tilting of the quadrupoles; this emphasizes the need for studying the jet sound pressure field in four dimensions ( $\mathbf{x}, t$ ) to better understand the mechanisms of noise generation.

**Theoretical Background** The expression for pressure due to vortex sound, observed at a point  $\mathbf{x} = (x_1, x_2, x_3)$  in the acoustic far-field, can be written as

$$p^{(f)}(\mathbf{x}, t) = \rho_0 P_0^{(1)}(t_r) \frac{1}{r} + \frac{\rho_0 x_i}{c r^2} \frac{\partial^2}{\partial t^2} \Pi_i(t_r) + \frac{\rho_0}{c^2} \frac{\partial^3}{\partial t^3} Q_{ij}(t_r) \frac{x_i x_j}{r^3} + \dots, \text{ where} \quad (5.1)$$

$$P_0(t) = \frac{5-3\gamma}{12\pi} \frac{1}{c^2} \dot{K}, \quad K(t) = \frac{1}{2} \int V^2(\mathbf{y}, t) d^3\mathbf{y};$$

$$\Pi_i(t) = \frac{1}{8\pi} \int (\mathbf{y} \times \boldsymbol{\omega})_i d^3\mathbf{y}, \quad i = 1, 2, 3;$$

$$Q_{ij}(t) = -\frac{1}{12\pi} \int (\mathbf{y} \times \boldsymbol{\omega})_i y_j d^3\mathbf{y}, \quad i = 1, 2, 3, \quad j = 1, 2, 3.$$

Here  $t_r$  is retarded time,  $P_0$ ,  $\Pi_i$ , and  $Q_{ij}$  are monopole, dipole and quadrupole terms respectively.

There are two constraints on the quadrupole tensor  $Q_{ij}$ : (i)  $Q$  is symmetric and its diagonal components sum to zero and (ii) if the vorticity field is axisymmetric about the  $x_1$  axis, the off-diagonal components of the tensor must vanish and  $Q_{22} = Q_{33} = -2Q_{11}$ . If the vorticity does not remain symmetric in a plane, the integrals of vorticity in that plane and the corresponding off-diagonal components of the tensor *will not vanish*. Conversely, if the quadrupole has nonvanishing off-diagonal components, then the quadrupole and consequently the vortex rings are tilted.

**Results of inviscid simulation of tilted rings** Vortex rings were represented by vortex filaments of a given strength and core radius and their evolution (self and mutual inductions) was calculated using standard Biot-Savart methods (Leonard 1985). When the rings were initially identical and axisymmetric, the motion was the familiar leapfrogging of axisymmetric vortex rings. The sound computed from this motion had a strictly axisymmetric quadrupole directivity at all times (with fluctuating amplitude). If the rings were tilted by as little as 1% of their radii toward one another, the result was much different. Figure 5.1 is a representative frame. First of all, the rings no longer stayed planar and their angle of tilt changed direction with each leapfrog and increased in amplitude. Eventually they intertwined or ejected one another on divergent paths. Second, the sound they produced was essentially that of a tilted axisymmetric quadrupole, the angle of tilt swinging in the plane of the tilt of the vortices, *but with a much greater angle*. As the vortex rings became more nonplanar, the tilting quadrupole ceased to be axisymmetric and became bisymmetric. By the time the rings were significantly tilted, the sound field was a very complicated quadrupole and was swinging in direction as wildly as it was oscillating in amplitude.

The conclusion drawn from this exercise was that there is little wonder axisymmetric quadrupole directivity has not been observed before Bridges and Hussain (1992; hereafter BH1): even in experiments designed to spatially fix the pairing and measure its noise, the slightest asymmetry in the vortex motion causes a large asymmetry in the sound and smears the extinction angle. Only in the facility described in BH1 and used in the experiments described here, where the flow was exceptionally clean and axisymmetric, could the quadrupole be observed.

**Results from experiments with hemispherical microphone array** The experiments were conducted under two different excitation conditions, namely stable double pairing (SDP) and stable pairing (SP), using various excitation amplitudes. Here only the results from the SDP flow at an excitation amplitude of 0.7% will be reported. The jet velocity was 26.7 m/s ( $M=0.08$ ) and the excitation frequency of 921.4 Hz corresponded to a Strouhal number based on jet diameter of 1.38. The SDP situation was similar to the one used and extensively documented in BH1. Under this excitation condition two pairs of axisymmetric vortices are formed and merge and the resultant vortices pair again before breaking down into a highly three-dimensional vortical structure. This motion produces a distinct subharmonic and a quarterharmonic tone in the far-field. The sound data was acquired by the 16 microphones (Figure 5.2) simultaneously at a rate 10 times the excitation frequency; 64 records of 1024 points each were obtained for each microphone.

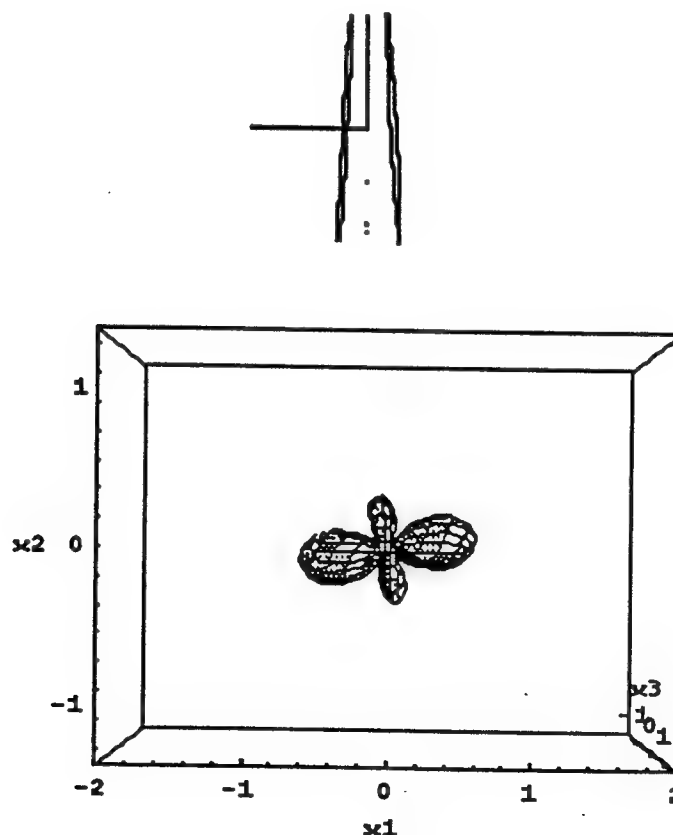


Figure 5.1 Pairing of tilted vortex rings and their sound field. A representative frame showing the tilted rings and the resultant directivity (represented by an equal-pressure surface).

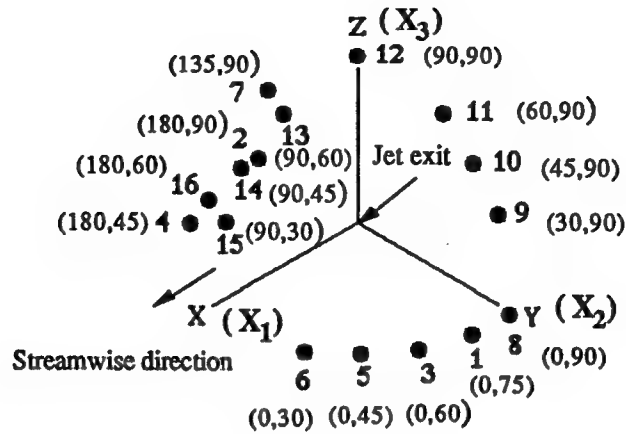


Figure 5.2 Microphone placements. The numbers in brackets refer to polar location  $(\theta, \phi)$ . Microphones 8, 1, 3, 5, 6, 4, 16, 2, 7 are in XY plane, microphones 12, 13, 14, 15 are in XZ plane, and microphones 8, 9, 10, 11, 12 are in YZ plane.

**Time evolution of three-dimensional jet sound field** Data were analyzed with different bandpass filters applied ( $f_{ex}/4$  and  $f_{ex}/2$ ) over the same duration in time; here we concentrate on the filtered ( $f_{ex}/4$ ) data. From representative time traces of the  $f_{ex}/4$  signal recorded at three azimuthal location in the exit plane of the jet one can discern that the sound field is not truly axisymmetric at this frequency. Large variations in both phase and amplitude are evident; this suggests that there is significant variation in the symmetry of the sound field. The time-averaged spatial coherence was relatively good at this frequency, however, allowing a measurement of phase using the transfer function between microphones.

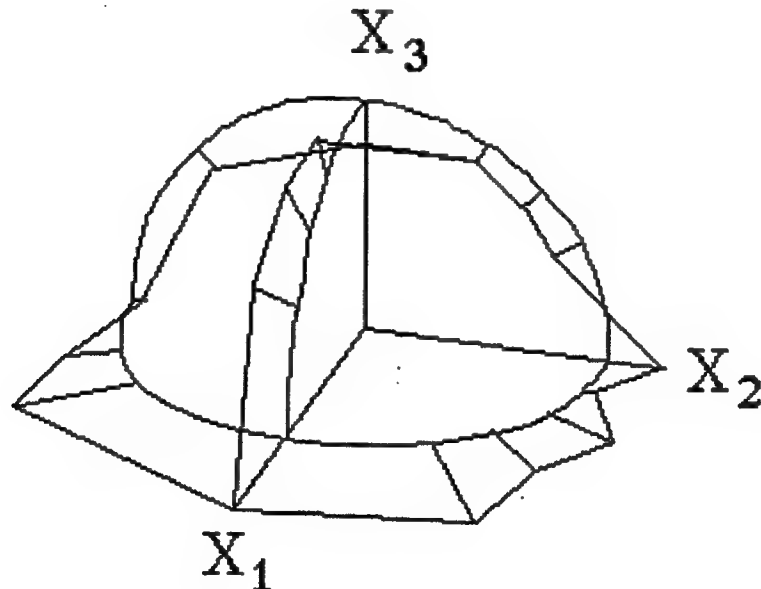


Figure 5.3. A representative frame from bandpassed ( $f_{ex}/4$ ) sound data records of stable double pairing. Jet axis is  $x_1$ -axis; quarter sphere frame is zero pressure.

**Directivity of the jet sound field** The instantaneous sound data was studied graphically on an isometric drawing of the microphone array by drawing a radial line segment whose length represented the sound pressure at each microphone (Figure 5.3). Liberties were taken to interpolate, using a weighted average of the three nearest points, a sound pressure at the jet axis. This allows a connected line between these points which makes it easier for the viewer. The radius of the quarter sphere coordinates indicates pressure equal to 0; when the line segment is drawn in toward the axis, the pressure is negative. A few frames from the movie containing  $f_{ex}/4$  data is shown in Figure 8. Note the extinction angle in the polar plane which often appears near  $\phi = 65^\circ$ , as was found in the time-averaged data, and the lack of such an extinction angle in the azimuthal ( $\theta$ ) plane.

**Multipole decomposition** To interpret the large experimental dataset, the multipoint sound pressure records are fitted by a multipole decomposition of the far-field pressure. Note that this is very different from conventional source location techniques which represent the source terms as a spatial distribution of monopoles. Such a representation is not physically relevant to particular aeroacoustic source mechanisms, which are intrinsically quadrupole in nature.

A general linear regression model of the form

$$p = M + x_i D_i + x_{ij} Q_{ij} \quad (2)$$

was used to fit the data, where the  $x_1$  axis corresponds to the jet axis.  $M$ ,  $D_i$  and  $Q_{ij}$  represent the monopole, dipole and quadrupole coefficients, in that order. Due to limitations in the number of microphones available and the expectation that their contribution is small, the dipole components in directions normal to the jet axis ( $D_2$ ,  $D_3$ ) were set to zero.

Figure 5.4 shows the relative magnitudes of the primary components,  $M$ ,  $D_1$ , and  $Q_{11}$ , as a function of time. The dipole and quadrupole terms are generally in phase with each other, while the monopole term is usually larger and out of phase with the dipole and quadrupole terms. Figure 5.5 shows how the off-diagonal components of the quadrupole tensor change with time. They are an order of magnitude lower than the primary components and exhibit significant differences in phase.

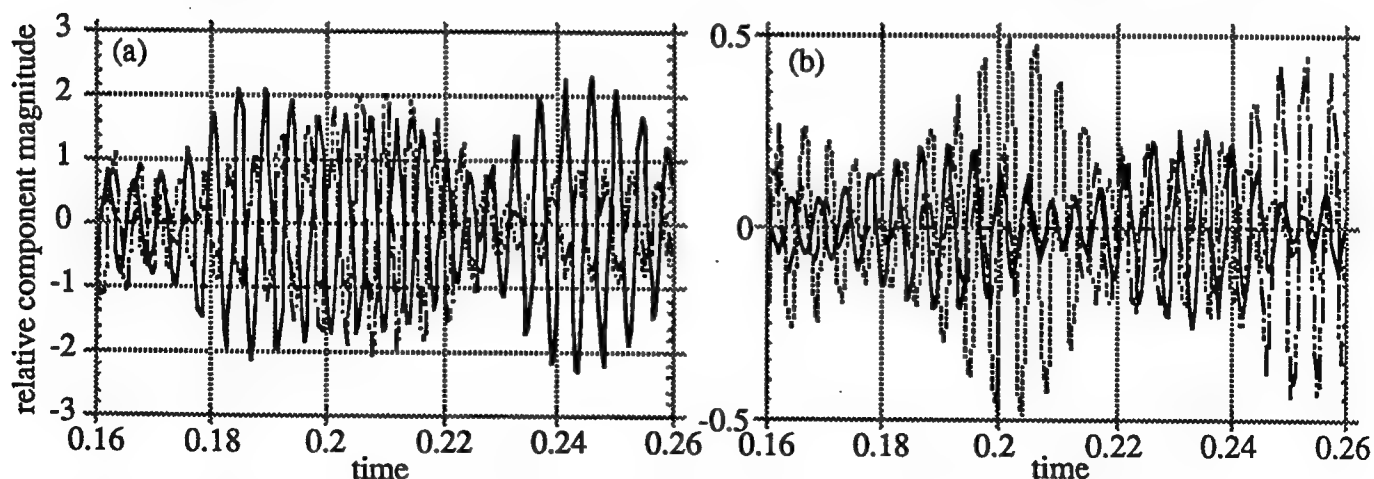


Figure 5.4. Fitted multipole components: (a) primary coefficients: ——— monopole, ..... axial dipole, - - - - - axisymmetric quadrupole 11; (b) off-diagonal quadrupole coefficients: ——— quad12, ..... quad13 and - - - - - quad23, indicating tilting from axisymmetry.



**Conclusions** We have studied the three-dimensional, time-dependent sound pressure field produced by vortex pairing in a jet, concentrating on variations from axisymmetry caused by deviations from axisymmetry in the vorticity field. We have used vortex filament simulations and vortex sound theory to explain these findings. These studies are examples of the kind of experiments we feel will greatly aid understanding of the physical mechanisms of jet noise production in the future. A few points about the work should be emphasized.

- The theoretical result that axisymmetric vortex motion must produce axisymmetric quadrupole directivity is *independent* of the details of the interaction, such as vorticity distributions within the vortex cores, etc. This is a fundamental result of vortex sound theory. A complementary finding of this study is that the sound field is very sensitive to the symmetry of the vorticity field and small deviations from axisymmetry result in large variations in the sound field directivity.

- The observations made here explain why sound field features such as azimuthal coherence and quadrupole directivity are not found in time-averaged measures of the jet sound field. Ribner's (1978) remarks that "the demonstrated absence of axisymmetry in the broad band correlation rules out any significant role for axisymmetric source structures." show that the crux of the matter is to clarify what is meant by "axisymmetric source structures". The lack of these time-averaged features does not prove that near-axisymmetric vortex motions are unimportant; on the contrary, they are direct results of the sensitivity of the sound field to vortex field symmetry. Practical axisymmetric vortical structures in jets and their interactions may still play a significant role in the production of jet noise; however, in order to recognize this role, the lack of symmetry which also plays a key role in their observed effect must be taken into account. This study also sheds light on the observation that the jet sound field is comprised of "fluctuating beam pattern sweeping randomly" earlier reported by Maestrello and Pao (1975). The observed 'beams' may have been the lobes of tilting quadrupoles.

- This type of study of jet noise sources is unlikely to result in actual prediction of magnitudes of the noise in practical jets anytime soon—at least not before the vortex dynamics of turbulent flows are more fully understood.

- Multipole decomposition of instantaneous sound data, as dictated by vortex sound theory, was useful here in correlating source and sound and reaching our conclusions regarding the possible role of vortex pairing in jet noise. This approach may be used to advantage for other vortex motions in the future, especially through combined efforts of specialized experiments and computational studies of vortex motions and sound.

## 6. Kinematic Separation of Homogeneous Mixtures

Previously, we reported the puzzling phenomenon of separation of components from an initially uniform mixture (air and smoke) in a rotating flow device (a cylindrical can with a rotating end disc). We further studied this phenomenon through experiments, analysis of particle forces, and direct numerical simulation (DNS). Separation of spherical polystyrene particles when immersed in water or pure alcohol lends further credence to the phenomenon. We have studied the dependence of the particle-free column size and its establishment time on particle size, particle concentration, disc and cylinder Reynolds numbers, and *fluid composition*. The evolution of passive markers in DNS shows segregation similar to that observed in experiments, supporting our kinematic separation hypothesis. However, kinematic action, though important, is inadequate to explain the "anti-diffusion" phenomenon. Although estimates show that *known* particle forces cannot account for the particle separation, experimental results suggest the action of an unknown lift force whose effect is magnified kinematically in our apparatus. At high particle concentrations or when a small amount of solute (*e.g.* sugar, salt, alcohol) is added to water polystyrene particle mixtures, the flow within the column becomes unstable and the particle-free column loses its axial symmetry; this unusual behavior is not yet clearly understood.

## References

- Narayanan, S. 1994 Spatiotemporal dynamics in a forced plane mixing layer. M.S. Thesis, University of Houston.
- Melander, M. V. & Hussain, F. 1993 Core dynamics on a vortex column. *Fluid Dyn. Res.* 10(b),1.
- Bridges, J., and Hussain, F. 1992, "Direct evaluation of aeroacoustic theory in a Jet," *Journal of Fluid Mechanics*, Vol. 240, pp 469–501.
- Maestrello, L. and Pao, S.P. 1975 "New evidences of the mechanisms of noise generation and radiation of a subsonic jet," *Journal of Acoustical Society of America*, Vol. 57, pp 959–960.
- Ribner, H.S. 1978, "Two point correlations of jet noise," *Journal of Sound and Vibration*, Vol. 56(1), pp. 1–19.

## C. Plans for Next Year's Research

Future plans are indicated in §B in the individual reports. This is the final year of this grant.

#### **D. ONR Data Base Information**

(Publications/Patents/Presentations/ Honors Report: 01 October 1993 through 30 September 1994)

R&T Number: 4322480

Contract/Grant Title: N00014-89-J-1361/Basic studies in turbulent shear flows

Scientific officer: L. P. Purtell

Principal investigator: Fazle Hussain

Mailing address: University of Houston Mechanical Engineering Dept. 77204-4792

Phone number: (713) 743-4545

Fax number: (713) 743-4544

E-Mail address: mecelw@jetson.uh.edu

- |  |    |
|--|----|
| (i) Number of papers submitted to refereed journals but not yet published<br>(submitted or in press) (list attached) | 4  |
| (ii) Number of papers published in refereed journals (list attached)   | 9  |
| (iii) Number of books or chapters submitted but not yet published  | 0  |
| (iv) Number of books or chapters published   | 0  |
| (v) Number of printed technical reports & nonrefereed papers   | 0  |
| (vi) Number of patents filed   | 0  |
| (vii) Number of patents granted  | 0  |
| (viii) Number of invited presentations at workshops or professional<br>society meetings (list attached)              | 10 |
| (ix) Number of presentations at workshops or professional society<br>meetings (list attached)                        | 3  |
| (x) Honors/Awards/Prizes for Contracts/Grants Employees  | 0  |
| (xi) Demographic information about research personnel.   |    |

PI/CO-PI: TOTAL 1

Female: none

Minority: none

Grad Stdnts.: TOTAL: 5

Female: none

Minority: none

Post Doc: TOTAL: 1

Female: none

Minority: none

- (xii) Degrees Granted (list attached): 5

#### **E. Technology Transfer**

None

## F. List of Publications/Reports/Patents/Graduates

### 1. PAPERS PUBLISHED IN REFEREED JOURNALS:

Hussain, H. S. & Hussain, F. "Elliptic Jets. Part 3. Dynamics of Preferred Mode Coherent Structure" *J. Fluid Mech.* **248**, pp. 315-361 (1993).

Hussain, F. & Melander, M. V. "Model coherent structure dynamics: vortex reconnection core dynamics and interaction with turbulence" *Vortex Flows and Related Numerical Methods* (eds.: J.T. Beale, G.-H. Cottet & S. Huberson) Kluwer Acad. Publ., pp. 239-264 (1993).

Hussain, F., Virk, D. & Melander, M. V. "New studies in vortex dynamics: incompressible and compressible vortex reconnection, core dynamics, and coupling between large and small scales", *Sadhana: Proc. Indian Acad. Sci.* **18**, pp.477-529 (1993).

Hussain, F. "New approaches to vortex dynamics: core dynamics, helical waves, and interaction with fine scales", in *Eddy Structure Identification in Free Turbulent Shear Flows* (eds. J. P. Bonnet & M. N. Glauser), Kluwer Acad. Press, pp. 13-25 (1993).

Jeong, J., Grinstein, F. F., Hussain, F. & Albanis, N. "Eduction of coherent structures in a numerically simulated plane wake", in *Eddy Structure Identification in Free Turbulent Shear Flows* (eds. J. P. Bonnet & M. N. Glauser), Kluwer Acad. Press, pp. 65-75 (1993).

Broze, G. & Hussain, F. "Non-linear dynamics of forced transitional jets: Periodic and chaotic attractors" *J. Fluid Mech.* **263**, pp. 93-132 (1994).

Broze, G. & Hussain, F. "Nonlinear dynamics of forced transitional jets: temporal attractors and transition to chaos" in *Nonlinear Stability of Nonparallel Flows* (eds. S. P. Lin, W.R.C. Philips, & D.T. Valentine) Springer-Verlag pp 459-473 (1994).

Schoppa, W., Hussain, H. S. & Hussain, F. "Nonlinear instability of free shear layers: sub-harmonic resonance and three-dimensional vortex dynamics" in *Nonlinear Instability of Nonparallel Flows* (eds. S. P. Lin, W.R.C. Philips, & D.T. Valentine) Springer-Verlag pp 251-280 (1994).

Jeong, J. & Hussain, F. "On the identification of a vortex," *J. Fluid Mech* (in press)

Hussain, H., Hussain, F. & Goldshtik, M. "Anomalous separation of homogeneous particle-fluid mixtures: further observations", (submitted to Physical Review E) 1994.

Schoppa, W., Hussain, F. & Metcalfe, R.W. "A new mechanism of small-scale transition in a plane mixing layer: core dynamics of spanwise vortices," (submitted) 1994.

Broze, G. & Hussain, F. "Transitions to chaos in a forced jet: intermittency, tangent bifurcations and hysteresis," (submitted) 1994.

Narayanan, S. & Hussain, F. "Measurements of spatiotemporal dynamics in a forced plane mixing layer," (submitted) 1994.

### 2. BOOKS (AND SECTIONS THEREOF) PUBLISHED

None

### 3. TECHNICAL REPORTS, NON-REFEREED PAPERS:

Julin, E., Metcalfe, R. & Hussain, F. "Numerical Treatment of Mass Action Term in Pseudospectral Calculations of Chemically Reacting Flows", *Bull Am. Phys. Soc.* 38, p. 2214 (1993).

Husain, H., Goldshtik, M. & Hussain, F. "Striking Phenomena in a Rotating Can", *Bull Am. Phys. Soc.* 38, p. 2273 (1993).

Goldshtik, M., Hussain, F. & Shtern, V. "Rudiments of a theory of structural turbulence", *Bull Am. Phys. Soc.* 38, p. 2296 (1993).

### 4. PRESENTATIONS

"A new mechanism for transition in free shear layers: vortex core dynamics", *Symposium on Developments in Fluid Dynamics and Aerospace Engineering*, Bangalore, India, Dec. 9-10, 1993.

"Topological Fluid Mechanics and Vortex Reconnection", *Turbulence as a Problem in Physics*, Nehru Center for Advanced Scientific Research, Bangalore, India, Dec. 13-18, 1993.

"Chaos in Spatially Developing Mixing Layers", *Turbulence as a Problem in Physics*, Nehru Center for Advanced Scientific Research, Bangalore, India, Dec. 13-18, 1993.

"Anomalous diffusion in fluid-particle mixtures", *Turbulence as a Problem in Physics*, Nehru Center for Advanced Scientific Research, Bangalore, India, Dec. 13-18, 1993.

Six lectures on "Eddy Structure Identification Techniques for Free Turbulent Flows" *International Center for Mechanical Sciences*, Udine, Italy, May 23-27, 1994.

### 5. PATENTS GRANTED

none

### 6. DEGREES GRANTED

Shashi Menon, December 1994, MSME.

Nikolaos Albanis, December 1994. MSME.

Satish Narayanan, May 1994, MSME.

Wade Schoppa, May 1994, MSME.

Arindam Ghosh, May 1994, MSME.

## **G. List of Awards/Honors/Prizes**

None

## **H. Other Sponsored Research**

**TITLE:** Innovative Studies of Turbulent Combusting Flows: Holographic Velocimetry and Numerical Simulation

**SPONSOR:** ONR

**AWARD AMOUNT:** \$336,205 (-\$110 balance)

**START DATE:** 3/15/93

**END DATE:** 9/30/94

**TITLE:** Development of HPV to Study Turbulence Near Free Surfaces

**SPONSOR:** ONR

**AWARD AMOUNT:** \$160,159 (\$387 balance)

**START DATE:** 4/1/93

**END DATE:** 3/31/95

**TITLE:** 3D Vector Wavelet-Based Subgrid-Scale Model for LES of Nonequilibrium Turbulence

**SPONSOR:** ONR

**AWARD AMOUNT:** (1/2 of) \$60,000

**START DATE:** 2/21/94

**END DATE:** 2/20/95

**TITLE:** Compressible Vortex Dynamics and Turbulence: Reconnection, Core Dynamics and Fine-Scale Organization

**SPONSOR:** NSF

**AWARD AMOUNT:** \$110,757

**START DATE:** 8/15/94

**END DATE:** 7/31/95

**TITLE:** Vortex Core Dynamics, Complex Helical Wave Decomposition, Organization of Fine-Scale Turbulence and Other Related Theoretical Studies

**SPONSOR:** AFOSR

**AWARD AMOUNT:** \$203,774

**START DATE:** 4/15/94

**END DATE:** 4/14/95

**TITLE:** Aluminum Fuel Combustion Chamber and Vortex Liquid Piston Engine

**SPONSOR:** ARPA

**AWARD AMOUNT:** (1/3rd of) \$189,720

**START DATE:** 5/15/94

**END DATE:** 11/14/95



TITLE: Aluminum Fuel Combustion Chamber and Vortex Liquid Piston Engine  
SPONSOR: ARO (AASERT)  
AWARD AMOUNT: \$219,687  
START DATE: 9/15/94  
END DATE: 9/14/97

TITLE: Acquisition of Advanced Instrumentation for Research in Turbulence, Chaos, Combustion and Two-Phase Flows  
SPONSOR: NSF  
AWARD AMOUNT: \$385,000 (equipment)  
START DATE: 10/1/94  
END DATE: 9/30/96

TITLE: High-Performances Data Acquisition and Control System for Dynamical Systems and Coherent Structures Approaches to Turbulence  
SPONSOR: NSF  
AWARD AMOUNT: \$40,000 (equipment)  
START DATE: 10/1/94  
END DATE: 9/30/95

### **I. Funding Balance**

A major issue at ONR is expenditure rates. Not meeting Navy required expenditure rates will result in redirection of resources within ONR for FY95 that starts on 01 October 1994! I would like to enlist your help in preventing this from occurring. If your expenditure rate is below that required by your contractual arrangement with ONR, we will be forced to delay funding increments in your contract/grant, even if the delay is due to slow billing from your business office. If the problem is at your business office, please take action to correct it.

Indicate the remaining ONR grant/contract resources you have in your institution as of 30 SEP 94:

\$111 remain from a total award of \$627,317 for the period 12/01/88 to 9/30/94.